

1-1-2002

## A study on material detachment mechanism in CMP process

Wei Che  
Iowa State University

Follow this and additional works at: <https://lib.dr.iastate.edu/rtd>

---

### Recommended Citation

Che, Wei, "A study on material detachment mechanism in CMP process" (2002). *Retrospective Theses and Dissertations*. 19814.

<https://lib.dr.iastate.edu/rtd/19814>

This Thesis is brought to you for free and open access by the Iowa State University Capstones, Theses and Dissertations at Iowa State University Digital Repository. It has been accepted for inclusion in Retrospective Theses and Dissertations by an authorized administrator of Iowa State University Digital Repository. For more information, please contact [digirep@iastate.edu](mailto:digirep@iastate.edu).

**A study on material detachment mechanism in CMP process**

by

**Wei Che**

A thesis submitted to the graduate faculty  
in partial fulfillment of the requirements for the degree of  
**MASTER OF SCIENCE**

Major: Mechanical Engineering

Program of Study Committee:  
Abhijit Chandra, Co-major Professor  
Ashraf Bastawros, Co-Major Professor  
Palaniappa A. Molian

Iowa State University

Ames, Iowa

2002

Copyright © Wei Che, 2002. All rights reserved.

Graduate College  
Iowa State University

This is to certify that the master's thesis of  
Wei Che  
has met the thesis requirements of Iowa State University

Signatures have been redacted for privacy

---

## Table of Contents

|  |      |
|--|------|
| Table of Contents .....  | iii  |
| List of Figures .....  | vi   |
| List of Tables .....   | viii |
| Abstract .....   | ix   |
| Chapter 1 Introduction and Literature Review .....                             | 1    |
| 1.1 Introduction.....  | 1    |
| 1.2 Background and literature review .....                                     | 2    |
| 1.2.1 Types of mechanical model during CMP process .....                       | 3    |
| 1.2.2 Existing model for MRR.....  | 5    |
| 1.2.3 Some speculations for material removal mechanism during CMP process..... | 8    |
| Chapter 2 Objectives of this Research.....                                     | 10   |
| Chapter 3 Cross – Scratch Experiment .....                                     | 11   |
| 3.1 Objectives of the scratch experiment.....                                  | 11   |
| 3.2 Experimental set up.....   | 13   |
| 3.3 Experimental step and data analysis procedure .....                        | 16   |
| 3.3.1 Experimental procedure .....   | 16   |
| 3.3.2 Data analysis procedure .....  | 18   |
| 3.4 Experimental calibration for load cell set up .....                        | 20   |
| 3.4.1 Theory of calibration for loading point.....                             | 20   |
| 3.4.2 Calibration for loading direction.....                                   | 25   |
| 3.4.3 Correction for RC delay.....   | 26   |

|   |    |
|---|----|
| 3.5 Experimental result.....  | 27 |
| 3.5.1 Characteristic length under certain indentation depth .....                   | 27 |
| 3.5.2 Normal indentation force under certain depth .....                            | 33 |
| 3.5.3 The ratio of tangential force to normal force during sliding indentation..... | 34 |
| 3.6 Experimental data sheets.....   | 34 |
| Chapter 4 A Mechanical Model for MRR during CMP .....                               | 39 |
| 4.1 Frame work of model development .....   | 41 |
| 4.2 Number of intersections per unit area per unit time .....                       | 42 |
| 4.2.1 Number of particles per unit area and inter-particle distance .....           | 42 |
| 4.2.2 Number of intersections per unit area per revolution .....                    | 43 |
| 4.2.3 Typical concentration definition .....  | 46 |
| 4.3 The average local pressure applied on the solid-solid contact region .....      | 48 |
| 4.3.1 Asperity model.....   | 49 |
| 4.3.2 FEM model .....   | 51 |
| 4.4 Normal force per particle .....   | 52 |
| 4.4.1 Full contact model.....   | 52 |
| 4.4.2 Partial contact model.....  | 52 |
| 4.4.3 Beam model .....  | 53 |
| 4.5 Indentation depth of a single particle.....                                     | 53 |
| 4.5.1 Perfect plasticity model (Plastic contact and small indentation): .....       | 53 |
| 4.5.2 Hardness test model .....   | 54 |
| 4.6 Tangential force acting on the active particles. ....                           | 55 |
| 4.6.1 Model based on orthogonal cutting.....  | 55 |

|  |    |
|--|----|
| 4.6.2 Experimental model.....  | 58 |
| 4.7 Characteristic length during the intersections at right angle..... | 58 |
| 4.7.1 A simple mechanistic model.....                                  | 58 |
| 4.7.2 FEM result.....  | 60 |
| 4.8 Volume per intersection.....                                       | 61 |
| 4.9 MRR model.....   | 61 |
| 4.9.1 Existing MRR model.....  | 61 |
| 4.9.2 Present Intersection model.....                                  | 62 |
| Chapter 5 Conclusion and Future Work.....                              | 66 |
| 5.1 Conclusion.....  | 66 |
| 5.2 Future Work.....   | 67 |
| References.....  | 69 |
| Acknowledgement.....   | 72 |

## List of Figures

|   |    |
|---|----|
| Figure 1.1 Schematic of CMP Polisher.....   | 1  |
| Figure 1.2 Surface profile of a single scratch. ....  | 9  |
| Figure 3.1 An ideal figure to show the purpose of this experiment.....  | 12 |
| Figure 3.2 Flowchart for cross-scratch experiment .....   | 14 |
| Figure 3.3 Experimental set up for cross-scratch experiment.....  | 15 |
| Figure 3.4 a) is the digital image of a typical sample surface. b) is used to show the length<br>measured. ....   | 18 |
| Figure 3.5 A schematic of calibration for load cell set up. ....  | 22 |
| Figure 3.6 Experimental calibration curves for sensitivities and cross-sensitivities along y-<br>axis. ....   | 24 |
| Figure 3.7 Experimental calibration curves for sensitivities and cross-sensitivities along x-<br>axis. ....   | 25 |
| Figure 3.8 Experimental calibration curves for tension and compression.....   | 26 |
| Figure 3.9 A typical force curve along a secondary scratch showing 3 intersections. ....  | 28 |
| Figure 3.10 Tangential force response close to intersection zone, showing different decay<br>rates. ....  | 28 |
| Figure 3.11 Figure (a) shows the intersecting scratches. Figure (b) shows the transition from<br>plowing to shearing. Dimpling is evident with the shear zone. .... | 29 |
| Figure 3.12 An intersection close to free edge. ....  | 30 |
| Figure 3.13 The force curve for the scratch intersecting with free edge. ....   | 30 |
| Figure 3.14 Tangential force response close to intersection with free edge.....   | 31 |

|  |    |
|--|----|
| Figure 3.15 Characteristic length variation with scratch depth. ....   | 31 |
| Figure 3.16 Surface profile of the cross-section of a scratch.....   | 32 |
| Figure 3.17 Normal force variation with indentation depth. ....  | 33 |
| Figure 4.1 A typical flow diagram for MRR. ....  | 41 |
| Figure 4.2 A schematic of particle motion in CMP process.....  | 44 |
| Figure 4.3 A schematic of particle train motion with unit cell. ....   | 44 |
| Figure 4.4 SEM image of an IC 1000 pad. The pad surface is tilted 60° to show the relative<br>surface topography.....                        | 48 |
| Figure 4.5 Orthogonal cutting process shows that two mechanism of ploughing and shearing.<br>.....   | 55 |
| Figure 4.6 (a) FEM abrasive particle-surface interaction model. (b) Normal and tangential<br>reaction forces on the abrasive particles. .... | 60 |
| Figure 4.7 A schematic of wafer pad contact area.....  | 62 |
| Figure 4.8 Comparison between model predictions and the copper CMP data with pressure.<br>.....  | 64 |
| Figure 4.9 Comparison between model predictions and the copper CMP data with<br>velocity.....  | 65 |

## List of Tables

|   |    |
|---|----|
| Table 1 Experimental data sheet of experimental set up calibration for loading point along x, y direction (The unit for the sensitivities is mv/gm).....      | 34 |
| Table 2 Experimental data sheet for experimental set up calibration for loading direction along x, y direction (The unit for the sensitivities is mv/gm)..... | 35 |
| Table 3 Experimental data sheet for characteristic length variation with indentation depth..  | 36 |
| Table 4 Summary statistics of two data sets for ratio of tangential force to normal force. ....   | 38 |
| Table 5 Comparisons for different assumptions.....  | 57 |

## Abstract

Chemical Mechanical Polishing (CMP) is the process of planarizing the surface aided by the combined force of the chemical etching and mechanical polishing. The unique feature of CMP is its global planarization of the non-planarized surface, which always occurs in the process of microelectronics fabrication. It has been found that CMP works extremely well in planarization process, and has a widespread application in many materials. However, the material removal mechanism (MRM) in CMP process is not well understood, and a theoretical model for prediction of material removal rate (MRR) is not fully developed.

The overall objective of this research is to study the material removal mechanism of the ductile metal surface during this micro and nano-polishing process, and develop a mechanical model to predict the MRR under certain situations. The abrasion process of pure copper surfaces is studied by a cross-scratch experiment in micro range. The experimentally observed deformation pattern by SEM and the trends of the measured force profiles reveal that, for an isolated scratch, the material is mainly plowed along the track of the indenter, and there is no net material removal along the trench of the surface. However, it is observed that material is detached close to the intersection zone of two scratches. It is speculated that the deformation mechanism changes from ploughing mode to shearing mode as the indenter approaches the intersection of two scratches under small indentation depth for ductile metals. And the characteristic length of the detached segment is found to be of the same order as the indentation depth. Such result is also justified by FEM results and Molecular Dynamics studies. A mechanism based material removal rate (MRR) model is then developed for CMP process. The predicted MRR values are comparable to the experiment data.

## Chapter 1 Introduction and Literature Review

### 1.1 Introduction

The initiative of pushing IC technologies forward is continually increased device density or shrunk dimensions of electronic devices, and one of the critical step during IC fabrication process is the photolithography, which requires a very planar surface for fabrication consideration. CMP refers to chemical mechanical polishing (or planarization) process, which causes planarization of surface. It has become the most promising method in this area because of its demonstrated ability to provide good global planarization and better local planarization of working surface.

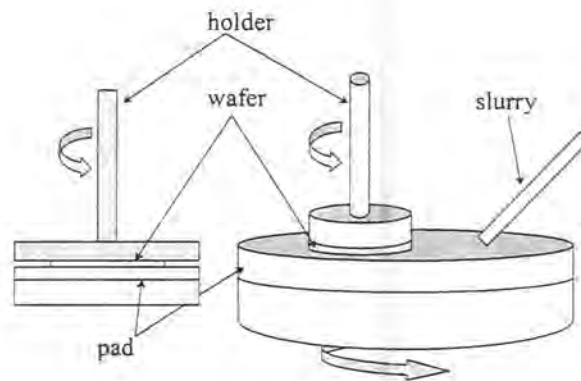


Figure 1.1 Schematic of CMP Polisher.

The CMP process mainly consists of wafer, pad, abrasive particles, and slurry. The general setup of CMP process is shown in Fig 1.1. A wafer rotates about its axis while being face down by a holder against a rotating polishing pad covered by the slurry containing abrasive

particles. The wafer surface faced down to the pad is the working surface to be polished. The pad is used to provide the support against the wafer surface, and carry slurry containing abrasive particles and chemical agent. The abrasive particles in the slurry are used as the mechanical cutting tool, which cut the surface material, and the chemical agent is used to soften the material surface or etch the selective material. The slurry flow will bring the removed material out of the working area.

CMP process has wide applications in modern industry. In VLSI fabrication, it is usually used to polish the oxide (usually silicon oxide), which is used as ILD (interlayer dielectric), and metals (such as copper, tungsten and aluminum) used to form interconnections between layers and layers. It can also be used in front-end applications in silicon IC fabrication, such as polishing poly-silicon films or photoresists, or post-end applications.

## **1.2 Background and literature review**

The CMP process is quite complicated, involving a large numbers of variables. The main output parameters could be MRR. High MRR process is used to polish thicker films, and low MRR process for thinner films for the purpose of control. The other important considerations in the final results of CMP process include surface quality, surface damage and planarization rate. And the real planarization is the subtraction of high feature MRR and low feature MRR.

The input variables for CMP process is too complicated, and it maybe divided according to wafer, pad, abrasive particles and slurry. The operation parameters like pressure and rotational speed are also very important, and they are always one of the interests for most researchers.

Wafer size, wafer curvature, the film hardness and microstructure are main parameters in the wafer. Wafer size play a role in the feed rate of slurry and integrity of the abrasive particles under the wafer, and wafer curvature will affect the pressure distribution under the wafer. Mechanical damage on the film is directly related to the film hardness, and film microstructure will influence its chemical behavior.

Polish pad is very important since it will interact with most of the input variables. Pad surface geometric properties and material properties are two things to be considered. Pad fiber structure and pore size will affect the transport of the slurry and the by-product in the process and the local pressure of the pad. Pad elastic modulus and hardness will affect the surface quality of the wafer. Generally stiffer and hard pad are expected to provide good planar surface, and soft pad is expected to give defect-free surface. Pad compressibility is also a critical issue. A more compressible pad gives long-range conformality and better uniformity, and a low compressibility is desirable for planar surface.

For abrasives, usually silica and alumina are used in oxide polishing and metal polishing. The abrasive size and hardness are two important factors. A better control of the abrasives size and its distribution will give a smooth surface, and the hardness of abrasives will determines the effectiveness of abrasion.

The viscosity and chemical agents in the slurry will also influence the MRR. In this research, their influence to the process are not deeply explored, and it is assumed that they softens the wafer surface properties, like hardness and yield strength, to account for the chemical effect.

### **1.2.1 Types of mechanical model during CMP process**

It is known that the material removal in CMP occurs as a combination result of chemical and

mechanical effects. Most researches that have been done before treat them separately. For simplicity, only mechanical effects are considered in this work, and the chemical effects are taken into account by softening the material property.

Generally, there are two typical mechanical models in CMP process, lubrication model based on fluid mechanics and solid-solid contact model based on solid mechanics. In the former model, the pressure is usually very low, and fluid speed is very high. So the fluid inside the wafer and pad is thick enough that wafer and pad do not contact each other. The material removal is due to the fluid flow, and lubrication theory is used to formulate the shear force on the wafer surface. In this case, the mechanical effect of abrasive particles is not considered, so the MRR is very low. It is speculated that it could be a lower bound of MRR in CMP process. In the solid-solid contact model, the pressure is usually very high compared to the lubrication model, and fluid speed is very low. The material removal is due to repeated sliding, rolling and nano-indentation of the abrasives against the wafer surface, and Contact mechanics is used.

In real case, we may imagine that material removal is due to a combination of chemical effect and mechanical effect. The mechanical removal will interact with the chemical removal, and their effects will be enhanced each other. The chemical effect may be enhanced by mechanical abrasion, fluid flow and other factors in the mechanical removal. Chemical etching may also soften the mechanical parameters, such as hardness, yield strength. So a desired MRR model and planar surface are the combined results of chemical and mechanical effects.

### 1.2.2 Existing model for MRR

One of the most important parameters in CMP process is the material removal rate (MRR), and there are several MRR models for this process. The early models of CMP are from glass polishing technology, and it is derived by Preston (1927). MRR could be expressed as  $\dot{H} = C \cdot P \cdot V$  where,  $\dot{H}$  is the MRR, the average height removal/unit time, P is applied pressure, V is the relative velocity between the pad and the wafer, and C is a constant called Preston's coefficient. Preston's equation represents a wafer scale phenomenological model, where any other physical and chemical considerations are lumped into the Preston's coefficient. Although this kind of equation has been widely used in CMP process, it cannot show the effect of other parameters in this process. Recent experiment results have shown that pad properties, abrasive particles size and concentration all have large influences on MRR. So other models are required to make better explanations for this process

Brown (1981) has developed a mechanistic model for optical polishing of metals. They assume fully solid-solid contact, and they get a governing equation similar to the Preston's equation with Preston's coefficient to be  $1/2E$ .

Tseng and Wang (1997) propose a modification to the assumption of linearity in Preston's equation. They derive a feature scale model with  $\dot{H} \sim P^{5/6} \cdot V^{1/2}$  based on combined solid and fluid mechanics, and their model predictions fit very well with the experimental results of thermal oxides. Their formulation is mainly based on the model of Runnels and Eyman (1994), which propose  $\dot{H} \sim \sigma_n \tau$ , where  $\sigma_n$  is normal stress and  $\tau$  is shear stress. And this feature scale model is mainly about the effect of slurry flow. Based on fluid mechanics, they assume a 40 to 65 microns slurry film thickness in a CMP process in their formulation.

It is speculated that only a part of abrasive particles are involved in material remove process during CMP process, since the abrasive particles used in CMP process do have a normal distribution. Bulsara et al (1997) have developed a mechanistic model to determine the number of the abrasive particles involved in material removal, referred as active particles, and the normal force acting on a single active abrasive. They state that the forces are only transferred from the wafer to the pad by the active particles, and then the average force per particle could be derived. So their model could be used for hard pad or low pressure and high concentration. An interesting result is also got that the active particles are the tail end of the particle size distribution (less than 0.5% of the total abrasive particles). So they suggest that the abrasive particles with peaked size distribution should be used in CMP polishing process. Shi and Zhao (1998) develop a model for CMP process with soft pads. They also predict a nonlinear pressure dependence of MRR with  $\dot{H} \sim P^{2/3} \cdot V$ . It is shown that the fundamental mechanism of the pressure dependence of MRR with a soft a pad is totally different with a hard pad. Recently Zhao and Shi (2000) develop a new model with  $\dot{H} \sim (P^{2/3} - P_{th}^{2/3}) \cdot V$ . In this model, a threshold pressure is introduced, and only the pressure over this limit will cause material removal. Some experimental data fit well with this equation, but no better physical explanation support this threshold pressure. Also the fitting parameter involved in their equation is not dimensionless, which suggest that some other process parameters required to be accounted.

Luo and Dornfeld (2001) develop a particle scale model based on fully plastic contact among the wafer, abrasive particles and pad. They propose a new model with  $\dot{H} = CP^{1/2}V$ , and the interesting thing here is that C is not only related to the material parameters, but also related

to operation parameter, pressure. They build this relation by introduce the particle size distribution which is dependent on the applied pressure, and they assume a very hard pad here which may be in conflict with their soft pad assumption. Although there are some ambiguities, this is a new MRR model that gives a lot of considerations for material property and surface property of the pad, and some consideration for abrasives shape and size distribution.

Fu et al (2001) have developed a proposed plasticity based beam model to determine the relationship between the MRR and the various operation and design parameters, such as pressure, velocity, pad property, abrasive shape, abrasive size and abrasive concentration. It may be suggested that there are two different contact modes between the wafer, abrasive particles and pad, non-contact mode (applied force is transferred only by abrasive particles from the wafer to the pad) and contact mode (force is transferred by abrasive particles and pad in contact with the wafer). An analytical solution for this transition condition has also been derived. For this particle scale model, they have a model with  $\dot{H} \sim P^{3/2} \cdot V$  for non-contact mode, and  $\dot{H} \sim P^{9/8} \cdot V$  for contact mode. Their results have been well justified by comparing their MRR trend with pressure, velocity, particle size and concentration with several experiment data.

Bastawros et al (2002) develop a phenomenological model by numerical results to account for the pad effects. And they propose that three contact mode exists between wafer and pad, non-contact, partial contact and full contact, based on different applied pressure, pad modulus and slurry concentration. The predicted MRR relations with slurry characteristics are in agreement with the experiment trends.

However, the common thing of the early models is that their predicted MRR values are

usually several orders higher than the experimental value. They think the materials in the trenches are all removed as the particles move along. The differences between ploughing and cutting are not considered. The material removal mechanism, which will be explored in this work, is not investigated in depth.

### **1.2.3 Some speculations for material removal mechanism during CMP process**

The mechanism of wafer surface deformation under the abrasive particles is cutting, ploughing, or forming intermittent pileups with successive shearing, based on the study of Hokkirigawa et al (1988) and Gahilin et al (1998). The cutting process resembles macroscopic surface machining, wherein the surface material is detached through a micro-shear localization process. In the ploughing process, the surface material ahead of the abrasive particle is plastically flowing to the trench sides with no net material losses. A third mechanism has been also observed wherein the deformed surface material is piled ahead of the abrasive particle, and then it is sheared off, forming intermittent debris. The competition between these mechanisms depends on the applied loads, relative sliding velocity, the abrasive particle shapes, and the ability of material to withstand high plastic deformation without shear localization (material's ductility).

Generally fracture mechanism is predominant in brittle material, and plastic shearing mechanism is predominant in the polishing. Brown (1987) shows that the difference between two mechanisms can be triggered by different cutting depths and abrasive size. And the mechanism transitions could be explained by physico-chemical interaction. So in silicate materials, the transition from brittle to plastic may be explained in this way.

Tomozawa (1997) proposed a mechanism for oxide CMP. It is suggested that the plastic

deformation and hydration of oxides are the main mechanism. The surface is softened by friction heat, and further weakens by hydration. Then the abrasive particles easily scrape off the hydrated surface.

Zhao and Bhushan (1998) use SEM and TEM to study the material removal mechanism of single-crystal silicon on nano-scale. It is shown that at ultra-low loads, material is removed from a single-crystal silicon by abrasive wear with plastic deformation. At heavy normal loads, the material is primarily removed by a cutting process, like machining of ductile of metals

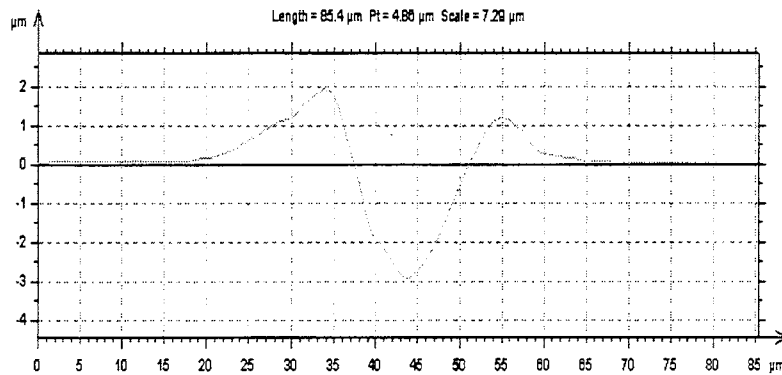


Figure 1.2 Surface profile of a single scratch.

Generally the abrasive particles track can be treated as a scratch. Fig 1.2 shows the surface profile of a single scratch, and it can be estimated that the area of the pileup is almost same to the that of the trench. It is speculated that there is no net material removal during a single scratch.

## Chapter 2 Objectives of this Research

The overall objective of this research is to investigate the material removal mechanism during the three-body contact, wafer, abrasive particles and pad during CMP process from mechanical consideration. The gained insights can be applied to develop a mechanically based MRR model to predict the material removal rate in CMP process.

The material is removed by plastic deformation for ductile metal under low loads, but how the material is removed under abrasive particles stills requires further investigation. It has been shown that the ploughing effect is very obvious in a single scratch, and it is suggested that no net material is detached. So a cross-scratch experiment is designed to study the material removal mechanism close to the intersection of two scratches.

The surface polishing process (CMP) is simulated by a micro-scale cross-scratch experiment. The experimentally observed deformation pattern by SEM image, surface topography by surface profilometer, and force profiles along the scratches on copper surfaces showed that the material is primarily ploughed during the scratch under the indenter, and there is little material detachment from the surface. However, it is observed that the material near the intersections of two scratches is sheared. So it is speculated that the deformation mechanism changes from ploughing mode to shearing mode over a characteristic length near the intersection zone. And this characteristic length is found to be in the order of the indentation depth at that mechanism transition point. And this idea is used to build the material removal rate model based on solid mechanics and contact mechanics.

## Chapter 3 Cross – Scratch Experiment

### Terminology:

$V_N$  : Normal voltage measured by the normal load cell (LC-N).

$V_T$  : Tangential voltage measured by the tangential load cell (LC-T).

$F_N$  : Normal force, acting normal to the LC-N and tangential to LC-T.

$F_T$  : Tangential force, acting normal to the LC-T and tangential to LC-N.

$S_{NN}$  : Sensitivity of normal load cell.

$S_{TT}$  : Sensitivity of tangential load cell.

$S_{TN}$  : Cross-sensitivity of LC-N due to LC-T.

$S_{NT}$  : Cross-sensitivity of LC-T due to LC-N.

a: Position length of a scratch.

l: The length of a scratch.

D: Diameter of grinding wheel.

d: Diameter of specimen.

h: Indentation depth of the indenter.

$L_c$  : Characteristic length

### 3.1 Objectives of the scratch experiment

The main purpose of this scratches experiment is to find the Characteristic length under certain indentation depth, and the Characteristic length is shown in Fig 3.1.

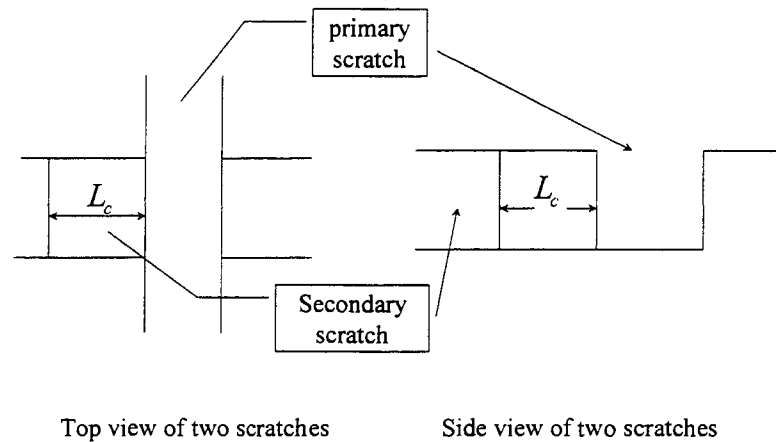


Figure 3.1 An ideal figure to show the purpose of this experiment.

During the experiment, as shown in Fig 3.1, two scratches that are perpendicular to each other are made. As the secondary scratch approaches the primary scratch (existing scratch), some phenomenon will occur after certain characteristic point. It is expected that the process will change from a steady ploughing state to an instability state. And it means that the material in the shaded region of Fig 3.1 will be sheared off, and this region is so called the instability region. The material before this region is the stable plowing region, and the pile up form along the scratch. And this mechanism transformation, from stability to instability, will be reflected by different force decay rate in the force diagram measured by the load cell transducers. So the geometric size of this region, Characteristic length, relative to the indenter depth could be found out. Also this cross-scratches experiment can be used to find the relationship between normal force and indentation depth, and the ratio of normal force to tangential force during this sliding indentation process.

## 3.2 Experimental set up

### Experiment apparatus

Grinding machine: Precision surface grinders (model 618 HYD).

Polisher: Ecomet 4 variable speed grinder-polisher from Buehler.

Indenter: Pencil point diamonds (with 45 degree semi-cone angle, 3/8in. \* 2 in. shank).

Transducer: ICP Force sensor, (model 208C01 with 10lb capacity).

Specimen: Pure copper (101 alloy series with 99.99% purity)

PC: Toshiba 700 CT laptop.

DAQ: DP 104 FFT Analyzer (20KHz bandwidth, maximum 51.2KHz sampling frequency).

Amplifier: PCB model 482A05.

Software: Dynamic Signal Analyzer.

Digital camera: PULNIX TM-6702.

Stereo-microscope: Nikon 109645.

The experimental flow diagram is shown in Fig 3.2. The first box is the instrument to do the cross-scratch experiment. The diamond indenter is installed on a grinding wheel, and the copper specimen and the transducer is fixed on the grinding machine base with magnetic force. The grinding machine provides the enough position control in x, y and z (12.5 micrometer resolution) direction, and base for the sensor. The second box is the transducer set up, which will measure the tangential force and normal force along the scratches. The load cells we used are general-purpose piezoelectric sensors that can be used to measure dynamic pressure and force. The measurement range is 10 lb for tension and compression. The upper frequency of load cell is 36 kHz, and minimum frequency is 0.01 Hz. The sensitivity under

axial loading is about 500 mv/lb. The third box is the signal conditioner to amplify the signal. The fourth box is our DAQ recorder setup. ACE DP104 FFT Analyzer is used in our experiment. It is a card that is slipped into a notebook PC, and has two input and two output channels. The maximum bandwidth is 20 KHz, and maximum sampling frequency is 51.2 KHz. The digital signal processor has a 50 MHz clock speed, with a 32 bit floating point format. The input parameters of ACE software are set up based on the user's manual of ACE software. The measurement parameters, like setting input to wait for the input trigger conditions, are set. The sampling parameters are set to determine the total time span the total data points. Also set the input channel parameters, like unit, range and delay and so on. So the data are captured in a controlled way and then the selected force signals are stored in the computer that will be post-processed.

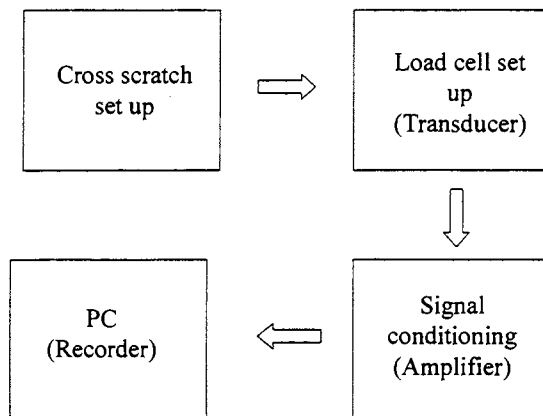


Figure 3.2 Flowchart for cross-scratch experiment.

The transducer (load cell) set up is shown in Fig 3.3. LC-N and LC-T are two piezoelectric

load cells with capacity 10 lb. They are used to measure the applied tangential and normal forces along the scratches (LC-N is under compression, so it will display positive signal. LC-T is under tension, so it will display negative signal), and they are fixed on the aluminum base with screws provided by the manufacturer. The aluminum block is used to hold the cylinder, and it will transfer the forces from cylinder holder to the two load cells. The copper cylinder is used to hold the specimen, and transfer the forces to two load cells. The copper specimen is fixed on the cylinder by double-side tape, and it only has one degree of freedom, rotation, which could give us control for scratch orientation. The conical diamond indenter with semi-cone angle of 90 degrees is used. The scratch is generated by rotating the spindle with the indenter around an axis parallel to the surface. The scratch depth is controlled by moving z direction of the grinding machine. The set up is calibrated with the accurate weight before doing any scratch experiment.

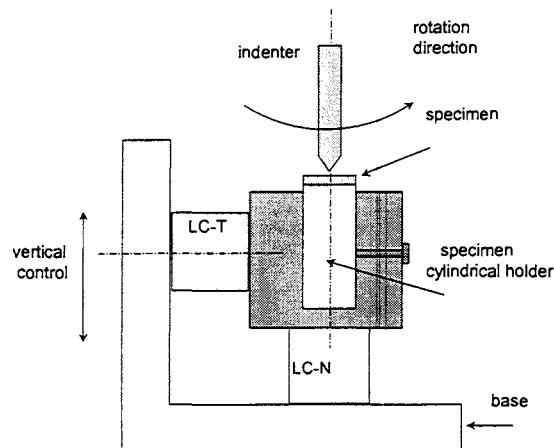


Figure 3.3 Experimental set up for cross-scratch experiment.

### 3.3 Experimental step and data analysis procedure

#### 3.3.1 Experimental procedure

Step1: Polishing the sample surface.

The polisher utilizes an electronic loading system to control the down force, which ranges from 1lb to 60 lbs. First of all, to keep the balance of specimen holder of polisher, mounted 3 or 6 copper specimens on the aluminum struts (specimen holder of polisher), then polishing one side of the sample surface, so that there are no micro-cracks on the surface under optical microscope at 80X magnification. The polishing procedure is usually followed by initial stages and final stages. The initial stages include sectioning, rough grinding and mounting. The final stages include fine grinding, rough polishing and final polishing. Based on our experiment conditions, only second stage is selected. 300grit and 600grit are used for rough grinding, and then abrasive particles with average size of 1  $\mu\text{m}$  are used for rough polishing. And the surface roughness is expected to be smaller than 1  $\mu\text{m}$  (actually can be up to 20 nm surface roughness) based on the experimental observation. The polishing process parameters are shown below.

Polishing particles:  $\alpha$  aluminum abrasive with average particle size 1  $\mu\text{m}$ .

Slurry: DI water.

Volume concentration: about 5%.

Down force control: 1 lb.

Rotational speed: 60-80 rpm.

Time: 5 – 7min for one cycle.

Rotational direction: Same for wafer and pad.

Mounted method: glue heated followed by water quench.

Clean method: 30 min ultrasonic clean with acetone liquid.

Step2: Make 3 primary parallel scratches.

Make 3 parallel scratches on the polished specimen surface. Those scratches are positioned right on the center by x and y control of grinding machine, and the distance between two scratches is about 2 mm so that there is no interacting influence between them. The scratch length is about 2 mm to 4 mm, with different depth. The range of maximum depth of one scratch is from 5 to 30  $\mu\text{m}$ , and the deeper scratches are made by multi-pass of the diamond tip. It is assumed that the torque is large enough that the rotational speed of the indenter is uniform during the experiment.

Step3: Polish the sample surface again to planarize the pile up along the scratches.

Take the specimen off from the measurement system. First mount the specimen on the polishing machine, then some hard filler is added in the scratch groove to avoid edge-rounding problem during the following polishing process. For simplicity we add some alumina abrasives in the multi-purpose glue as the filler, then fill the scratches with it. After a few hours, the fillers dry. Then polish it until the pile up along the trenches is polished off. The stereo-optical microscope is used to show if the pile up is planarized or not.

Step4: Make secondary parallel scratches,

Mount the sample again on the transducer set up. Do a series of scratches intersecting with the original three scratches with different depth. The secondary scratches are expected to be perpendicular to the original three parallel scratches. Record the output signals for secondary scratches with several intersections in the computer. Also record some signals for secondary scratches without intersections for comparisons.

Step5: Take a digital picture of the specimen with multiple scratches.

Take a picture of the sample surface with digital camera. Mark the scratch number and directions on the figure.

### 3.3.2 Data analysis procedure

Step1: Spatial coordinate measurement.

Measure the spatial coordinates of the starting and ending point of the scratch based on the digital image of the specimen. Assume that the center of the specimen is same as that of load cell, and take it as one-dimensional problem. The optical measurement is also calibrated with an accurate scale. The coordinate measurement is shown in fig 3.4.

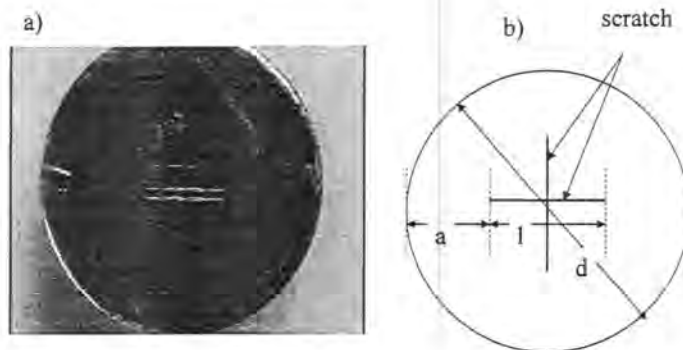


Figure 3.4 a) is the digital image of a typical sample surface. b) is used to show the length measured.

The length measured is “a”, position length of a scratch, “l”, length of a scratch, “d”: diameter of the specimen. And the spatial coordinate of the starting point is  $(a - d/2)$ , the spatial coordinate of the ending point:  $(a - d/2+l)$ . Those data are required to get the final

force from the output voltage data (refer to section 3.4.1).

Step2: Manage input data file for each scratch.

The signal caught for each scratch should be corrected to conform the format of the Matlab file (transform measured voltage signal to calibrated force signal). The measured total time span (40 ms) is not exactly relative to the scratch length in spatial span, but only part of them (about 10 ms). So the right data points should be taken out according to the scratch length.

Step3: Find the force by computation.

Transfer the voltage signal to the force signal for each scratch in the time space (Refer to 3.4.1).

Assume that the rotational speed of indenter is uniform, so that the parameters in the time space can be transferred to the spatial space.

Step4: Find the Characteristic length.

Find the Characteristic length on the force output diagram for each intersection based on the different force decay rate of the tangential force curve at the intersection point.

Step5: Find the indentation depth.

A rough estimation can be made based on the geometrical relation,  $h = \left(\frac{l}{2}\right)^2 / D$ .

Where  $l$  is the scratch length,  $h$  is the indentation depth, and  $D$  is the diameter of circle of the rotating track of indenter. Actually the indentation depths of the scratch at the intersection point are found with the profilometer, since the surface of the sample may be tilted and the surface roughness should be considered.

### 3.4 Experimental calibration for load cell set up

#### 3.4.1 Theory of calibration for loading point

Usually the load cell is designed to measure the axial load acting on it, and the loading point is expected to be right on the center of the load cell. In our experimental set up, except the axial loads, the radial loads and moments do exist, and the loading points are not right on the center, but on the load cell surface within some range of the center (shown in Figure 3.4). So these eccentric loads and moments will generate significant errors if the sensitivity of two load cells is not calibrated. So the first step of the experiment is to calibrate the two load cells around the surface under this design.

For axial loading right on the center,

$$V_N = S_N * F_N \quad (3.1)$$

$S_N$  is the sensitivity provided from the manufacturer.

In our experiment, the resultant forces can be treated as normal and tangential force that acts on certain point on the load cell surface. And also normal and tangential forces are applied at the same time. So the output of two load cells can be written as

$$V_N = S_{TN} * F_T + S_{NN} * F_N \quad (3.2)$$

$$V_T = S_{TT} * F_T + S_{NT} * F_N \quad (3.3)$$

The four parameters in the above equations can be determined in the following method.

Firstly apply axial load  $F_N$ , and  $F_T$  is not applied.

The loads applied are the accurate weight (100gm and 500gm weight). So forces are given, and output voltages can be measured. Then for each point on the surface,  $S_{NN}$  and  $S_{NT}$  are

given by

$$S_{NN} = \frac{V_N}{F_N} \quad (3.4)$$

$$S_{NT} = \frac{V_T}{F_N} \quad (3.5)$$

Secondly apply radial load  $F_T$ , and  $F_N$  is not applied, then  $S_{TT}$  and  $S_{TN}$  are given by

$$S_{TT} = \frac{V_T}{F_T} \quad (3.6)$$

$$S_{TN} = \frac{V_N}{F_T} \quad (3.7)$$

And these four parameters are all function of positions.

So equation (3.2) and (3.3) can be rewritten as matrix form as

$$\begin{pmatrix} V_N(x) \\ V_T(x) \end{pmatrix} = \begin{pmatrix} S_{NN}(x) & S_{TN}(x) \\ S_{NT}(x) & S_{TT}(x) \end{pmatrix} * \begin{pmatrix} F_N(x) \\ F_T(x) \end{pmatrix} \quad (3.8)$$

So if the output voltage curve is measured, the relative forces can be calculated based on the following equation for each point in the scratches.

$$\begin{pmatrix} F_N(x) \\ F_T(x) \end{pmatrix} = \begin{pmatrix} S_{NN}(x) & S_{TN}(x) \\ S_{NT}(x) & S_{TT}(x) \end{pmatrix}^{-1} \begin{pmatrix} V_N(x) \\ V_T(x) \end{pmatrix} \quad (3.9)$$

The four parameters in Eq. (3.9) are found based on the following step. The calibration set up is shown in Fig 3.5. The origin of the coordinates is right on the center of the circular copper plate, point 2 in Fig 3.5. Three loading points (point1, 2 and 3) are selected along the x-axis and y-axis on the sample surface. Tangential or normal load will be applied on each loading point. Four successive steps are used.

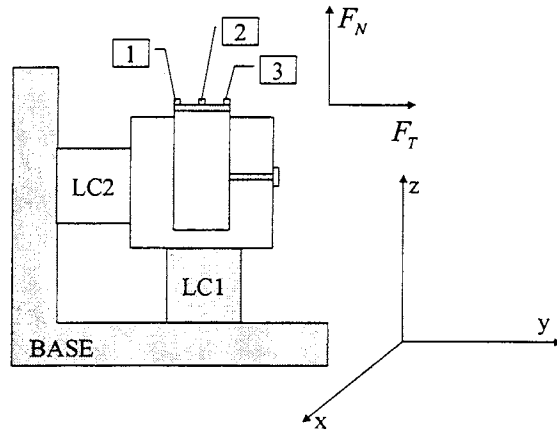


Figure 3.5 A schematic of calibration for load cell set up.

Step1: In the  $yz$  plane, apply normal load on point 1, with accurate weight of 100gm load and 500gm load. The relative voltage outputs are measured, and  $S_{NT}$ ,  $S_{NN}$  for point 1 are calculated based on Eq.(3.4) and (3.5). Then the data of  $S_{NT}$ ,  $S_{NN}$  for point 2 and 3 are got in a similar way.

Step 2: In the  $yz$  plane, apply tangential load on point 1,2,3, with accurate weight of 100gm load and 500gm load. The relative voltage outputs are measured, and  $S_{TN}$ ,  $S_{TT}$  for each point are calculated based on Eq.(3.6) and (3.7).

Step 3: In the  $xz$  plane, apply normal load on point 1,2,3, with accurate weight of 100gm load and 500gm load. The relative voltage outputs are measured, and  $S_{NT}$ ,  $S_{NN}$  for each point are calculated in a similar way.

Step 4: In the  $xz$  plane, apply tangential load on point 1,2,3, with accurate weight of 100gm load and 500gm load. The relative voltage outputs are measured, and  $S_{TN}$ ,  $S_{TT}$  for each point

are calculated.

Since the double scratches will be done in the yz plane, so the parameters from step1 and step 2 will be used in real calculation in the experiment. Step 3 and step 4 is used to check how much error could it be if the scratches are not right on the y-axis, but with some offset distance from the centerline.

The calibration curves for the four parameters along y direction are shown in Fig 3.6. The data points for 100gm load, 500gm load, and the average of the two with loading positions are plotted in the figure. The average values of the experimental data are used to do a linear fitting curve for each data set. It is easily to realize that a good linear relationship between sensitivities and the spatial position is observed. And also the difference between the sensitivities of this set up and the sensitivity under axial load (given by manufactures) is obvious. So this calibration is very necessary for this loading condition.

Based on linear regression method, the equation for  $S_{NN}$ ,  $S_{NT}$ ,  $S_{TT}$  and  $S_{TN}$  are give by

$$S_{NN} (V / Kg) = 3.47E - 02 * y(mm) + 0.945 \quad 3.11(a)$$

$$S_{NT} (V / Kg) = -7.35E - 03 * y(mm) + 4.31E - 02 \quad 3.11(b)$$

$$S_{TT} (V / Kg) = 1.38E - 04 * y(mm) + 0.5488 \quad 3.11(c)$$

$$S_{TN} (V / Kg) = -9.04E - 05 * y(mm) - 1.013 \quad 3.11(d)$$

Based on Eq (3.11), the sensitivity and cross-sensitivity along the y direction could be calculated, then the forces at any position could be calculated based on a simple product of matrix according to Eq (3.9). So the recorded voltage curve in time space could be transformed to force curve in time space.

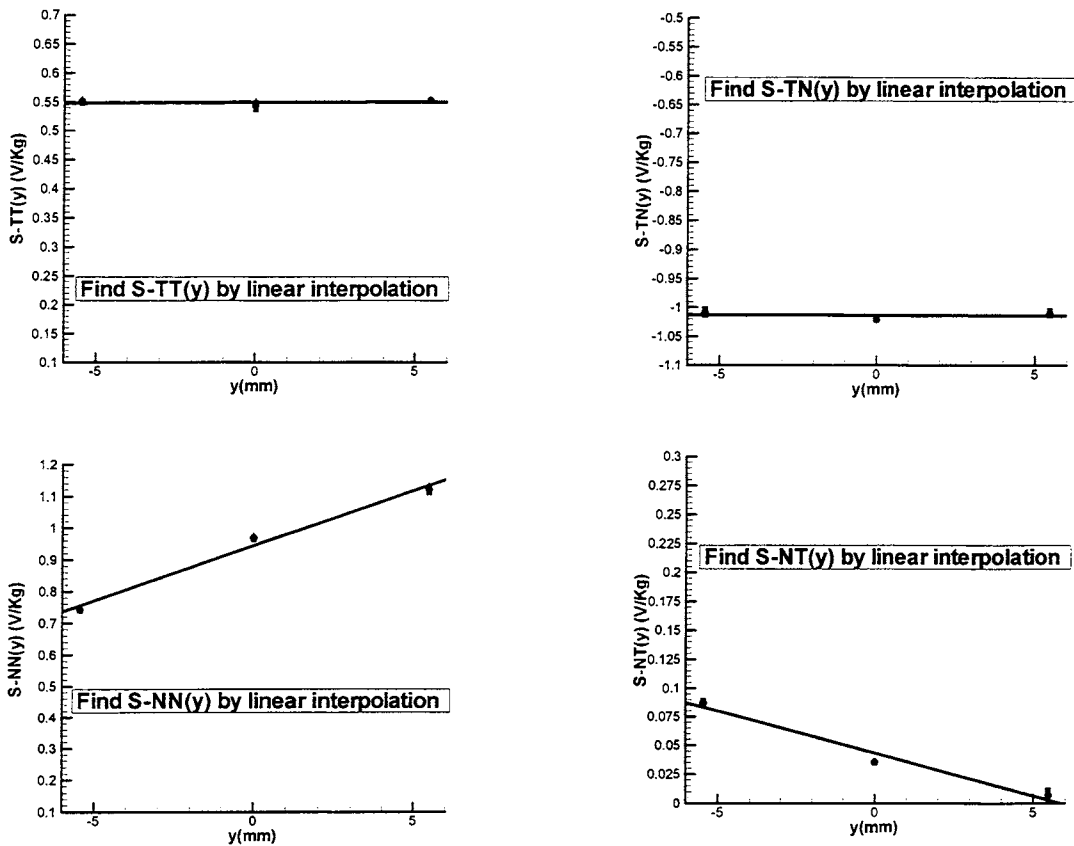


Figure 3.6 Experimental calibration curves for sensitivities and cross-sensitivities along y-axis.

The calibration curve along x direction is shown in Fig 3.7.

It can be seen that the values of sensitivity and cross-sensitivity does not change much along x direction, and the values of each parameter along x direction are similar to the values of the relative parameter on the center along x direction. And also the position of the scratches in our experiment is usually within 2 mm from the center. So it is reasonable to assume that the sensitivity and cross-sensitivity data are taken as one-dimensional data. And the data from calibration along y direction (Eq 3.11) will be used to calculate the forces based on the

voltage output.

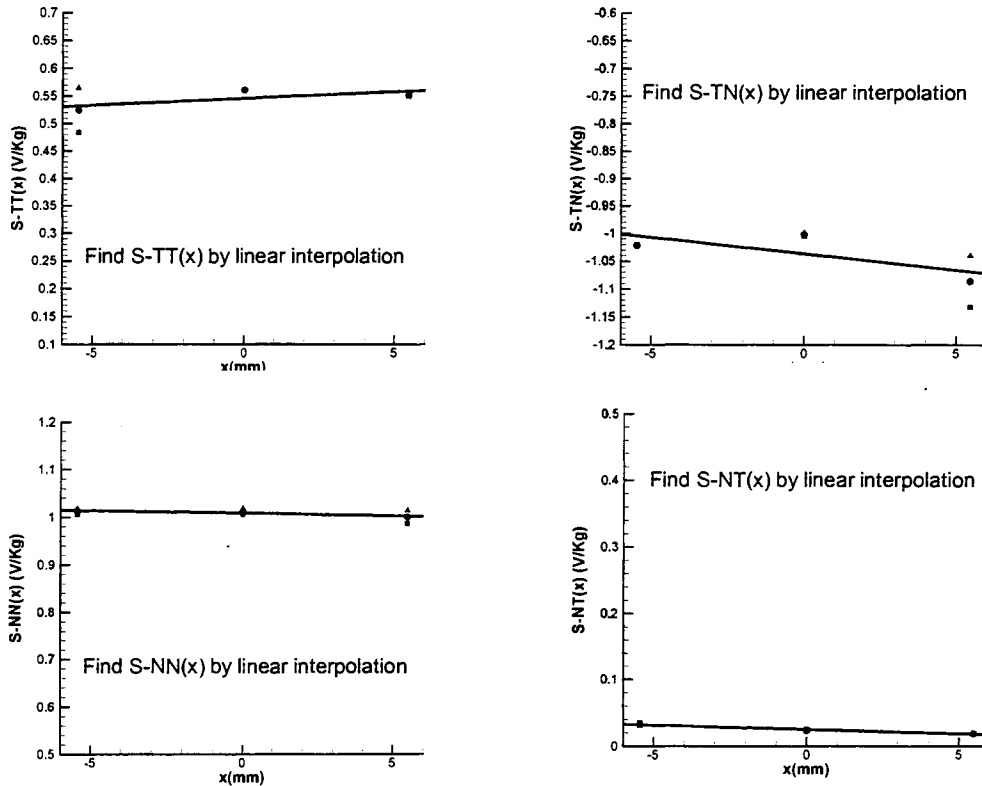


Figure 3.7 Experimental calibration curves for sensitivities and cross-sensitivities along x-axis.

### 3.4.2 Calibration for loading direction

Since the calibrations in 3.3.1 are done in the tension situations, but in our designed loading direction in the scratch experiment, one load cell is under tension, and the other is under compression. So the responses of load cell under tension and compression should be checked, even though they are supposed to be same amplitude except the negative sign (Positive for compression and negative for tension).

The calibration curve for loading direction is shown in Fig 3.8

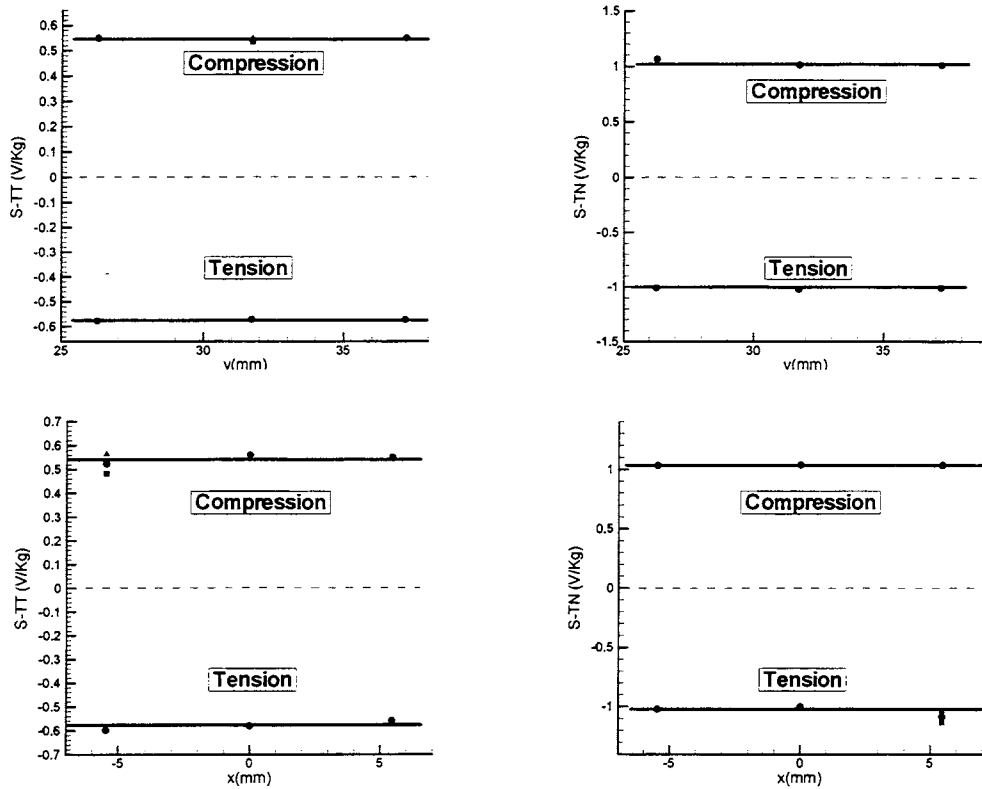


Figure 3.8 Experimental calibration curves for tension and compression.

Only  $S_{TT}$  and  $S_{TN}$  are checked in x and y direction, and  $S_{NN}$ ,  $S_{NT}$  are assumed to have the same response. And it is shown by Fig 3.8 that the response of tension and compression is same for our sensor set up.

### 3.4.3 Correction for RC delay

If the exerting force time is too long, it is expected to get overshoot problem. And based on the experiment, the delay time of our whole measurement system is about 0.78 seconds. Usually the time span of our experiment is within 20 ms. So the overshoot problem is not

really a problem in this experiment.

### **3.5 Experimental result.**

The main result is the characteristic length named for the length of the detached material segment close to the intersection of two scratches. It has been explored by the different force decay rate on the force profile, the SEM image of the intersections, and the surface profile of the single scratch. The relation between the normal force and the indentation depth, and the ratio of tangential force to normal force are also studied. The useful data are taken from six samples, and the data of 58 intersections are investigated. The scratch length is from 2mm to 4 mm., and the scratch depth is in the range of 1  $\mu\text{m}$  to 25  $\mu\text{m}$ . The time needed to do one scratch is within 40ms. The resolution per point is about 2 to 4  $\mu\text{m}$  per data point.

#### **3.5.1 Characteristic length under certain indentation depth**

The main purpose of this experiment is to find the Characteristic length under certain indentation depth. And it is done by find the mechanism transformation under force curve in time space or spatial space. Fig 3.9 is a typical force curve vs. time for a scratch. The normal force is positive, since it is under compression. The tangential force is negative, since it is under tension. The multiple ripples on the force curves are due to the dynamic response of the copper specimen fixture after scratch unloading at the intersection and then reloading again.

It can be seen that there are three intersections on this scratch. And the enlarged region for intersection 2 is shown on Fig 3.10. Several rates of the tangential force decays can be observed. Starting form the steady state ploughing process, as the secondary scratch

approaches the primary scratch, tangential force starts to drop since the surface is recessing near the primary scratch as a result of previous polishing.

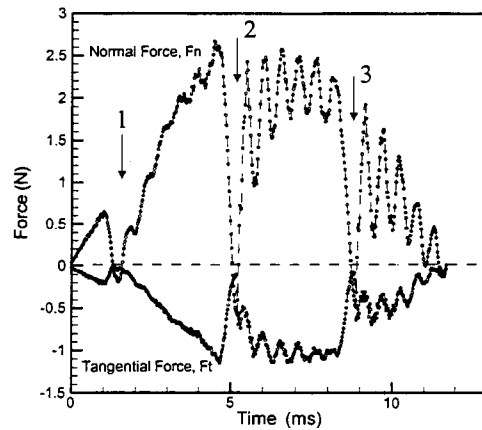


Figure 3.9 A typical force curve along a secondary scratch showing 3 intersections.

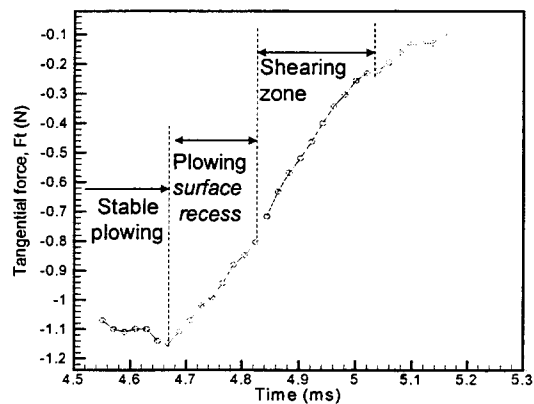


Figure 3.10 Tangential force response close to intersection zone, showing different decay rates.

Up to this point, the material is ploughed. Then, tangential force decays at a faster rate, which

we termed as a transition to shearing action. As the sheared segment falls into the primary scratch, the rate of tangential force drops until the sheared segment makes full contact with the other side of the primary scratches and subsequently, the tangential force starts to increase again.

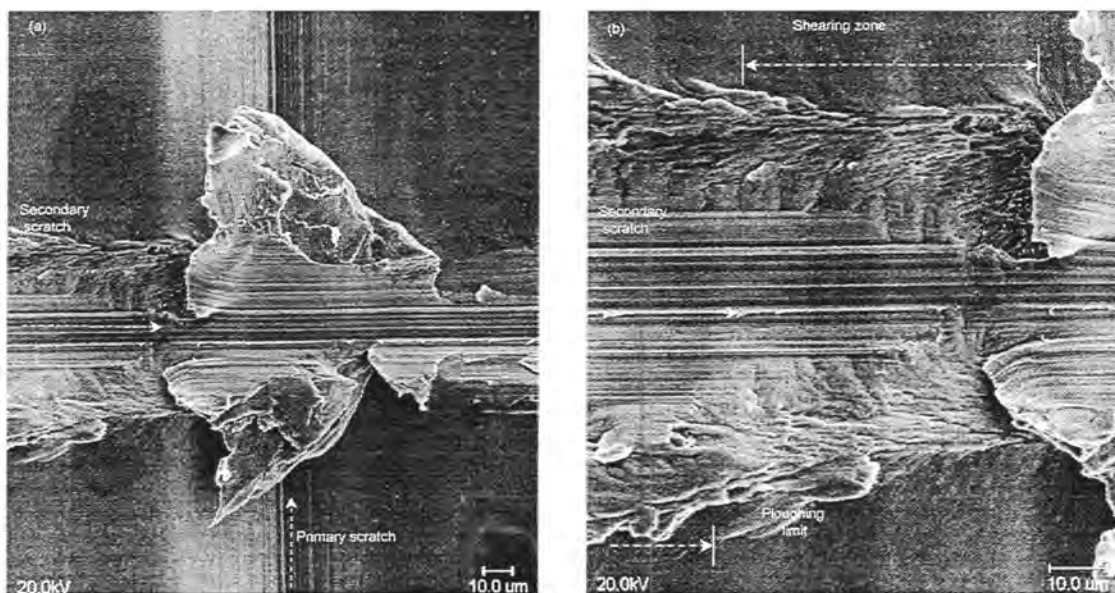


Figure 3.11 Figure (a) shows the intersecting scratches. Figure (b) shows the transition from plowing to shearing. Dimpling is evident with the shear zone.

The SEM image of this intersection is shown on Fig 3.11. A lot of materials are pushed into the trenches, and also the edge rounding appears on the edge of the scratch. Within the shearing zone, there is a lot of dimpling, which is an indication of plastic shearing.

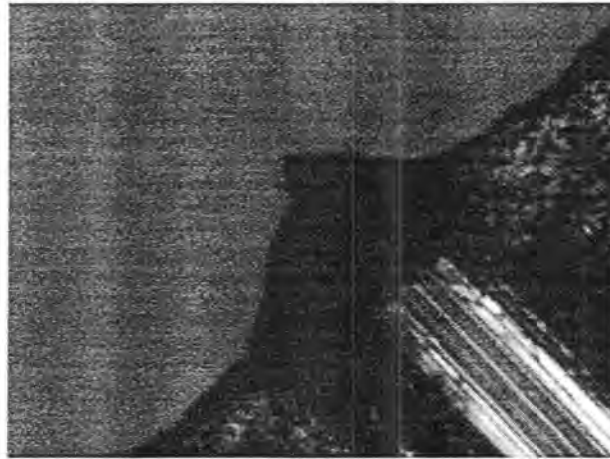


Figure 3.12 An intersection close to free edge.

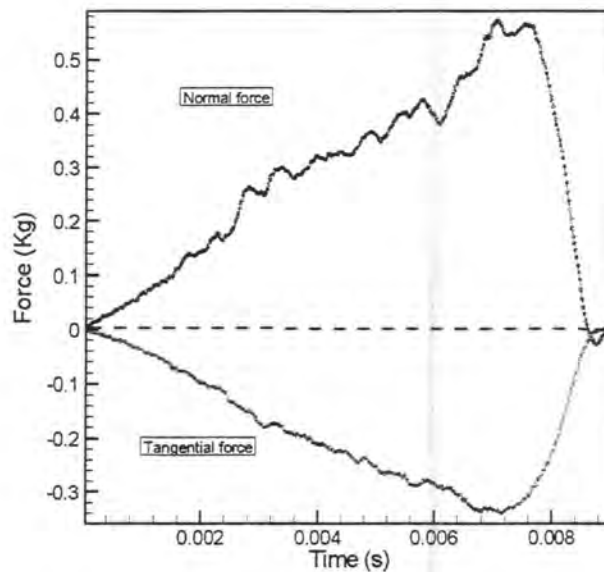


Figure 3.13 The force curve for the scratch intersecting with free edge.

This idea is further verified when we do a scratch intersecting with a free edge on the specimen. The digital image is shown on Fig 3.12, and the force curve of this scratch is shown in Fig 3.13. The force curve close to the intersection with free edge is shown in Fig 3.14. It is noticed that it is very similar to Fig 3.10, which also shows different force decay rate. And the plowing region and third region is because of the edge-rounding effect and the

resistance from the material ahead of the indenter, which is shown in the digital image of this intersection.

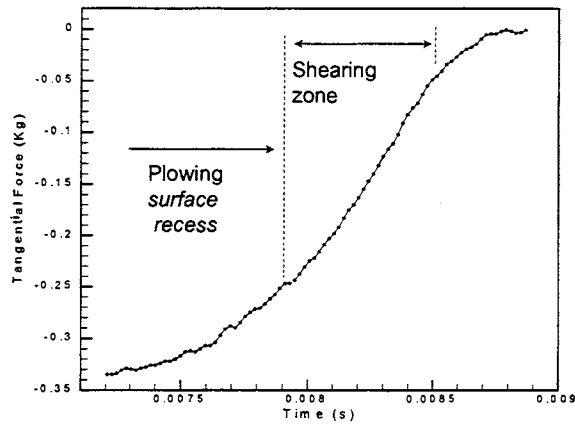


Figure 3.14 Tangential force response close to intersection with free edge.

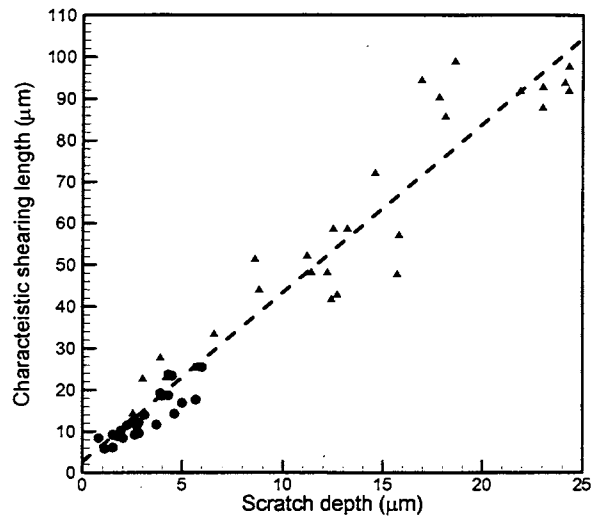


Figure 3.15 Characteristic length variation with scratch depth.

Based on this idea, the Characteristic length is extracted from the force curve, and it is shown

in Fig 3.15. A good linear relationship between Characteristic length and the indentation depth is observed. Actually there are two groups of data. One group has a large indentation depth, and the other has a relative small indentation depth. But the slopes of this two group are very similar. For simplicity, all data are fitted by one line. And the linear fitting equation for this curve is given by

$$L_c = 4.2h + 2.3 \quad (3.12)$$

Actually, characteristic length is about 3.7 times indentation depth based on each group data with a different intercept. It means that the Characteristic length is about 4 times the depth, which seems reasonable in common sense.

It is also observed that there is little material removed during steady plowing state. From the surface profile of the scratch, which is shown in Fig 3.16, the area of the pile up is nearly same as the area of the trench, which means that there is no net material removal during steady ploughing state.

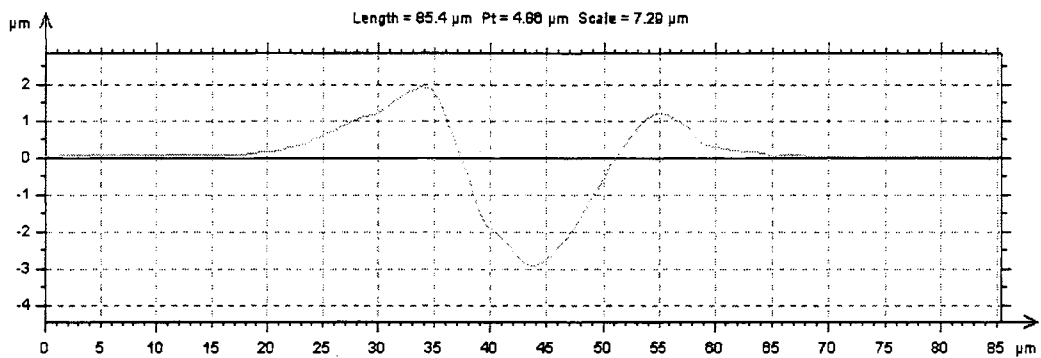


Figure 3.16 Surface profile of the cross-section of a scratch.

It is speculated that the material removal mechanism during sliding indentation (indentation depth is in micro-meter or sub micro size) is because of the intersection of two scratches from the view of mechanical consideration.

So the cross scratch experiment has provided a plausible mechanism of material detachment during surface polishing process. Even though the material is ploughed to the trench sides by the abrasive particles, a segment with length of the characteristic length is sheared off from the formed trench, when two trenches intersect each other.

### 3.5.2 Normal indentation force under certain depth

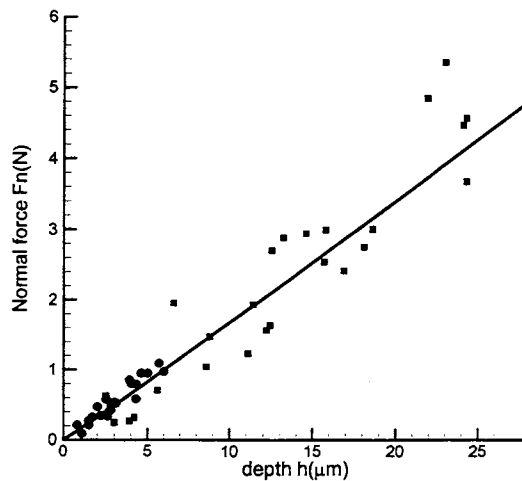


Figure 3.17 Normal force variation with indentation depth.

The normal indentation force is extracted from the point at which the instability occurs, because at this point the indentation depth is measured from profilometer. The normal force is got from the normal force measured. The relation between the normal force and indentation depth is shown in Fig 3.17. Two groups of data are shown in Fig 3.17, and with a

power fit for both of them. The fitting equation is given by

$$F_n = 0.1595h^{1.0207} \quad (3.13)$$

It can be seen that the normal force is nearly linearly depend on the indentation depth during sliding indentation process. And the other parameters, like hardness of copper, diamond indenter size, are plugged in the coefficient of Eq. (3.13), which has a dimension of  $N / \mu m$ .

### 3.5.3 The ratio of tangential force to normal force during sliding indentation.

The ratio of tangential force to normal force during sliding indentation is easily got from the output force data. Several scratches with no intersections are done, and the recorded signals are processed. It is shown in table 3 and table 4 for two data sets. The ratio is observed to oscillate within some range, and it can be a a constant during each process. Because of the complex response of the material, this ratio may very from 0.2 to 0.4 under certain indentation depth, or even larger. It is observed that for small indentation depth (less than  $10 \mu m$ ), 0.2 is the mean value, and 0.4 is the mean value for larger indentation depth (larger than  $10 \mu m$ ).

## 3.6 Experimental data sheets

Table 1 Experimental data sheet of experimental set up calibration for loading point along x, y direction (The unit for the sensitivities is mv/gm).

|           |       |       |       |           |       |       |       |
|-----------|-------|-------|-------|-----------|-------|-------|-------|
| x(mm)     | 0     | 0     | 0     | x(mm)     | 5.45  | 0     | -5.47 |
| y(mm)     | -5.45 | 0     | 5.47  | y(mm)     | 31.73 | 31.73 | 31.73 |
| S_TT(100) | 0.548 | 0.536 | 0.552 | S_TT(100) | 0.554 | 0.561 | 0.484 |
| S_TT(500) | 0.554 | 0.55  | 0.553 | S_TT(500) | 0.548 | 0.56  | 0.565 |

Table 1 (continued)

|           |        |        |        |           |        |        |        |
|-----------|--------|--------|--------|-----------|--------|--------|--------|
| S_TT(ave) | 0.551  | 0.543  | 0.5525 | S_TT(ave) | 0.551  | 0.561  | 0.5245 |
| S_TN(100) | -1.003 | -1.021 | -1.005 | S_TN(100) | -1.02  | -1.004 | -1.132 |
| S_TN(500) | -1.015 | -1.02  | -1.015 | S_TN(500) | -1.023 | -0.999 | -1.039 |
| S_TN(ave) | -1.01  | -1.020 | -1.01  | S_TN(ave) | -1.022 | -1.002 | -1.086 |
| S_NN(100) | 0.740  | 0.964  | 1.112  | S_NN(100) | 1.006  | 1.005  | 0.987  |
| S_NN(500) | 0.746  | 0.975  | 1.133  | S_NN(500) | 1.018  | 1.018  | 1.014  |
| S_NN(ave) | 0.743  | 0.969  | 1.122  | S_NN(ave) | 1.012  | 1.012  | 1.000  |
| S_NT(100) | 0.089  | 0.035  | 0.011  | S_NT(100) | 0.035  | 0.025  | 0.020  |
| S_NT(500) | 0.085  | 0.036  | 0.002  | S_NT(500) | 0.031  | 0.022  | 0.018  |
| S_NT(ave) | 0.087  | 0.035  | 0.007  | S_NT(ave) | 0.033  | 0.024  | 0.019  |

Table 2 Experimental data sheet for experimental set up calibration for loading direction along x, y direction (The unit for the sensitivities is mv/gm).

|                       |        |        |        |                       |        |        |        |
|-----------------------|--------|--------|--------|-----------------------|--------|--------|--------|
| x(mm)                 | 0      | 0      | 0      | x(mm)                 | 5.45   | 0      | -5.47  |
| y(mm)                 | 26.28  | 31.73  | 37.2   | y(mm)                 | 31.73  | 31.73  | 31.73  |
| S_TT_tension(100)     | 0.548  | 0.536  | 0.552  | S_TT_tension(100)     | 0.554  | 0.561  | 0.484  |
| S_TT_tension(500)     | 0.554  | 0.55   | 0.553  | S_TT_tension(500)     | 0.548  | 0.56   | 0.565  |
| S_TT_tension(ave)     | 0.551  | 0.543  | 0.553  | S_TT_tension(ave)     | 0.551  | 0.561  | 0.525  |
| S_TT_compression(100) | -0.577 | -0.569 | -0.573 | S_TT_compression(100) | -0.556 | -0.581 | -0.595 |
| S_TT_compression(500) | -0.576 | -0.573 | -0.572 | S_TT_compression(500) | -0.562 | -0.58  | -0.601 |

Table 2 (continued)

|                       |        |        |        |                       |        |        |        |
|-----------------------|--------|--------|--------|-----------------------|--------|--------|--------|
| S_TT_compression(avg) | -0.577 | -0.571 | -0.573 | S_TT_compression(avg) | -0.559 | -0.581 | -0.598 |
| S_TN_tension(100)     | -1.003 | -1.021 | -1.005 | S_TN_tension(100)     | -1.02  | -1.004 | -1.132 |
| S_TN_tension(500)     | -1.015 | -1.02  | -1.015 | S_TN_tension(500)     | -1.023 | -0.999 | -1.039 |
| S_TN_tension(avg)     | -1.009 | -1.020 | -1.01  | S_TN_tension(avg)     | -1.022 | -1.002 | -1.086 |
| S_TN_compression(100) | 1.067  | 1.013  | 1.011  | S_TN_compression(100) | 1.03   | 1.039  | 1.029  |
| S_TN_compression(500) | 1.06   | 1.016  | 1.011  | S_TN_compression(500) | 1.038  | 1.04   | 1.045  |
| S_TN_compression(avg) | 1.064  | 1.015  | 1.011  | S_TN_compression(avg) | 1.034  | 1.040  | 1.037  |

Table 3 Experimental data sheet for characteristic length variation with indentation depth.

| Sample and scratch # | Depth ( $\mu m$ ) | Characteristic length ( $\mu m$ ) | Sample and scratch # | Depth ( $\mu m$ ) | Characteristic length ( $\mu m$ ) |
|----------------------|-------------------|-----------------------------------|----------------------|-------------------|-----------------------------------|
| 1---1-1              | 3.0               | 28.2                              | 12---B-1             | 1.7               | 8.9                               |
| 1---1-2              | 17.8              | 90.3                              | 12---B-2             | 5.7               | 14.8                              |
| 1---2-1              | 8.6               | 51.4                              | 12---B-3             | NA                | NA                                |
| 1---2-2              | 18.1              | 85.7                              | 12---C-1             | 0.9               | 20.3                              |
| 1---2-3              | 16.9              | 102.9                             | 12---C-2             | 5.0               | 16.9                              |
| 1---3-1              | 8.8               | 43.9                              | 12---D-2             | 4.3               | 27.7                              |
| 1---3-2              | 18.6              | 87.8                              | 12---E-2             | 3.9               | 19.2                              |
| 1---3-3              | 6.9               | 98.8                              | 12---F-1             | 2.5               | 15.6                              |
| 2---1-3              | 5.6               | 25.3                              | 12---F-2             | 4.0               | 18.7                              |

Table 3 (continued)

|         |      |      |          |     |      |
|---------|------|------|----------|-----|------|
| 2---2-1 | 2.5  | 53.4 | 13---A-2 | 4.6 | 18.4 |
| 2---2-2 | 11.4 | 48.1 | 13---A-3 | 1.9 | 10.2 |
| 2---2-3 | 12.2 | 48.1 | 13---B-1 | 2.6 | 9.2  |
| 2---3-1 | 14.6 | 72.1 | 13---B-2 | 2.8 | 9.2  |
| 2---3-2 | 21.9 | 78.7 | 13---B-3 | 1.5 | 9.2  |
| 2---3-3 | 24.3 | 91.8 | 13---C-1 | 2.2 | 13.5 |
| 2---4-1 | 13.2 | 46.8 | 13---C-2 | 2.8 | 9.6  |
| 2---4-2 | 23.0 | 87.8 | 13---C-3 | 1.1 | 3.8  |
| 2---4-3 | 24.1 | 76.1 | 14---A-1 | 2.0 | 8.4  |
| 2---5-1 | 12.5 | 63.4 | 14---A-2 | 2.7 | 11.2 |
| 2---5-2 | 23.0 | 73.2 | 14---A-3 | 0.8 | 14.0 |
| 2---5-3 | 24.3 | 97.6 | 14---B-2 | 1.5 | 4.0  |
| 3---1-2 | 4.2  | 26.8 | 14---C-1 | 4.5 | 21.3 |
| 3---2-2 | 3.9  | 27.8 | 14---C-2 | 6.0 | 29.8 |
| 3---3-1 | 11.1 | 23.8 | 14---C-3 | 3.0 | 14.9 |
| 3---3-2 | 15.7 | 47.6 | 14---D-1 | 3.1 | 14.0 |
| 3---3-3 | 12.4 | 41.6 | 14---D-2 | 4.3 | 23.4 |
| 3---4-1 | 11.2 | 57.0 | 14---D-3 | 3.7 | 11.7 |
| 3---4-2 | 15.8 | 57.0 |          |     |      |
| 3---4-3 | 12.7 | 33.2 |          |     |      |

Table 3 (continued)

|          |     |      |  |  |  |
|----------|-----|------|--|--|--|
| 3---13-1 | 2.5 | 14.3 |  |  |  |
| 3---13-2 | 6.6 | 33.3 |  |  |  |

Table 4 Summary statistics of two data sets for ratio of tangential force to normal force.

| Sample2-scratch 2  |        | Sample12-scratch Z |        |
|--------------------|--------|--------------------|--------|
| Mean               | 0.3378 | Mean               | 0.2090 |
| Standard Error     | 0.0032 | Standard Error     | 0.0004 |
| Standard Deviation | 0.0247 | Standard Deviation | 0.0041 |
| Sample Variance    | 0.0006 | Sample Variance    | 0.0000 |
| Range              | 0.1144 | Range              | 0.0178 |
| Minimum            | 0.2720 | Minimum            | 0.2007 |
| Maximum            | 0.3864 | Maximum            | 0.2185 |
| Count              | 61     | Count              | 131    |

## Chapter 4 A Mechanical Model for MRR during CMP

### Terminology

$G$  is number of abrasives per volume

$W_a$  is total mass of abrasives.

$\rho_a$  is density of abrasives.

$Vol_a = \frac{\pi}{6} d^3$  is the average volume of a spherical particle.

$Vol_{slurry}$  is the volume of slurry.

$Vol_{water}$  is the volume of water.

$W_{slurry}$  is total mass of the slurry.

$\rho_{slurry}$  is density of the slurry.

$d_s$  is the dilution ratio, defined as the ratio of  $Vol_{slurry}$  to the sum of  $Vol_{slurry}$  and  $Vol_{water}$ .

$\alpha_m$  is the mass concentration of slurry before dilution which is defined as  $W_a / W_{slurry}$ .

$\alpha_v$ , or  $\alpha$  is the volume concentration of slurry before dilution.

is the mass concentration of slurry before dilution which is defined as  $W_a / W_{slurry}$ .

$N$ : is the total number of particles under the wafer.

$A_w$ : is the wafer surface area.

$d$ : is the average particle diameter.

$L_{p-p}$ : is inter-particle distance.

$u$  is the particle velocity relative to the wafer.

$\omega$  is the rotational speed of the wafer and pad.

$\beta_t$  is the trailing angle.

$x$  is the separating distance.

$N_e$  is effective cutting per unit time in defined square with inter-particle edge length.

$N_{rev}$  is effective cutting per revolution in defined square with inter-particle edge length.

$N_{in-p}$  is number of intersections left per revolution in the defined square.

$N_{in}$  is number of intersections left per revolution per unit area.

$E_w$  is the elastic modulus of wafer.

$E_p$  is the elastic modulus of pad.

$P$  is the assumed uniform pressure in the local summits of the pad

$P_0$  is the applied operating pressure.

$F_n$  is the normal force per particle.

$\sigma_y$  is the yield strength of material.

$h$  is the indentation depth of particles

$H$  is the hardness of material.

$F_s$  is tangential force on the shear plane.

$F_t$  is the thrust force (tangential force) acting on the abrasive(cutting tool).

$\phi$  is the shear angle.

$\beta$  is the friction angle on the chip-tool plane.

$L_c$  is characteristic length.

$A_c$  is the cross-section area.

The material removal rate (MRR) is a critical parameter in all the manufacturing process, and so for CMP process. The MRR of the CMP process is a combined result of chemical and mechanical effect. For simplicity only the mechanical model is built in here, and chemical effects are considered as a softening factor to material properties. And it is reasonable to realize that the material properties, such as surface hardness, yield strength, young's modulus, are changed by chemical effects.

#### 4.1 Frame work of model development

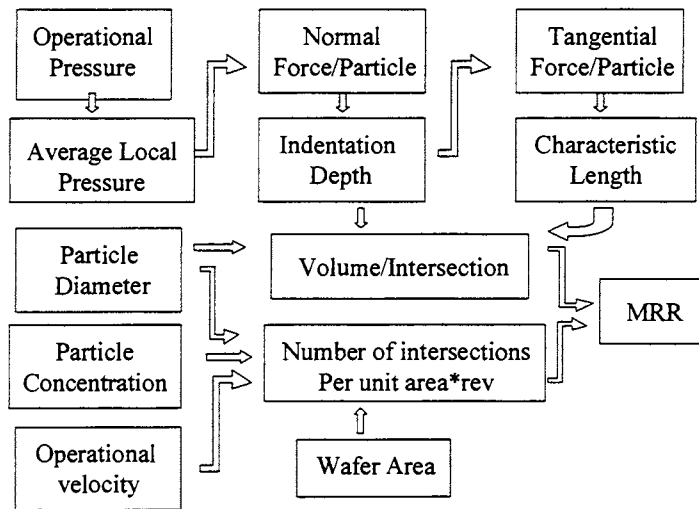


Figure 4.1 A typical flow diagram for MRR.

For solid-solid contact mode in CMP process, generally there are five important parameters in the procedure to determine the MRR: active particle numbers per unit area, average local pressure, normal force per particle, indentation depth, velocity of particle. Based on the

earlier work, some improvements are made to make the model more reasonable. And also three new extra parameters are proposed in our new model, those parameters are tangential force per particle, characteristic length during two intersecting tracks at right angle, number of intersections per unit area per unit time. The flow gram on how to determine MRR is shown in Fig 4.1. It is clearly to see that how each parameter influence MRR, and model procedure for each step is described below.

## 4.2 Number of intersections per unit area per unit time

### 4.2.1 Number of particles per unit area and inter-particle distance

A homogeneous volumetric concentration  $\alpha$  is assumed for the slurry used during the CMP process, and the average particle diameter is  $d$ . The linear velocity of particles relative to the wafer is also taken as a uniform value  $u$  across the whole wafer surface. During CMP process, the height of the slurry is assumed to be same as particle diameter  $d$ . So the volume concentration is given by

$$\alpha = \frac{N * V_{particle}}{A_w * d} \quad (4.2.1)$$

If not specified, all concentration considered here refer to volume concentration.

Where  $N$  is the total number of particles under the wafer, and  $A_w$  is the wafer surface area. If the particles are taken as spherical, Eq (4.1) can be rewritten as

$$\alpha = \frac{N * (\pi d^3 / 6)}{A_w * d} = \frac{N * \pi d^2}{6A_w} \quad (4.2.2)$$

At the particle scale,  $\alpha$  can be expressed in terms of inter-particle distance  $L_{p-p}$  with the same assumption of slurry height.

$$\alpha = \frac{\pi d^3 / 6}{L_{p-p}^2 * d} = \frac{\pi d^2}{6L_{p-p}^2} \quad (4.2.3)$$

So number of particles per unit area can be expressed as volumetric concentration and particle diameter or inter-particle distance

$$\frac{N}{A_w} = \frac{6\alpha}{\pi d^2} = \frac{1}{L_{p-p}^2} \quad (4.2.4)$$

Accordingly, the inter-particle distance can be expressed as volumetric concentration and particle diameter.

$$L_{p-p} = \sqrt{\frac{\pi d^2}{6\alpha}} \quad (4.2.5)$$

#### 4.2.2 Number of intersections per unit area per revolution

Fig 4.2 is a schematic of linear polisher showing the particles motion over the pad and the wafer. The particles are uniformly distributed around the pad, having the same speed with the pad, as shown in Fig 4.2. The wafer is rotating about its axis. A unit cell with edge length  $L_{p-p}$  in the wafer center is selected at time  $t$ , and it rotates to a new position at time  $t + \Delta t$ .

Fig 4.3 is the enlarged figure of unit cell showing the snapshot of this unit cell with time. The 1<sup>st</sup> particle represents the first particle of the particle train, and leaves a trench in the unit cell at time  $t$ . The other particles in this particles train will not form new trench, because the separation distance, which is  $x$  in Fig 4.3, is too small to form a new trench, and they just pass the unit cell along the formed trench by the 1<sup>st</sup> particle. When the separating distance exceeds a critical value, the  $i$ -th particle of the following particle train will form a new trench in this unit cell at time  $t + \Delta t$ . Same thing happens for the other particles of this train. It is assumed that each train forms one and only one trench, and has the same length (having same

number of particles). So the time interval to form a new trench is a constant, in other words, a new trench is formed after an angle of rotation of wafer. A simple model is developed to model the number of intersections per revolution per unit area formed by these trenches.

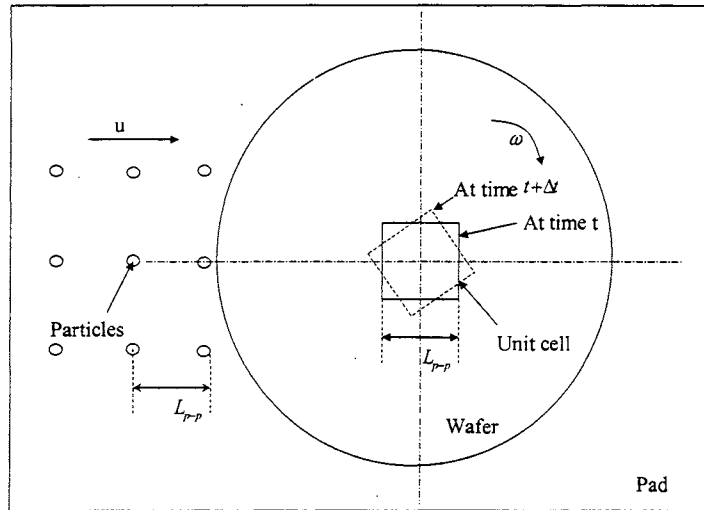


Figure 4.2 A schematic of particle motion in CMP process

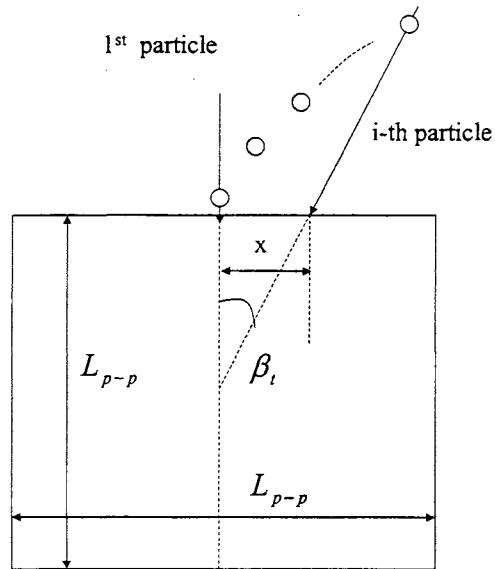


Figure 4.3 A schematic of particle train motion within unit cell.

If the height of slurry between wafer and pad is always taken as a constant  $d$ , particle

diameter, then the number of particles passing unit cell per unit time can be given as

$$J = \frac{u}{L_{p-p}} \quad (4.2.6)$$

So the number of particles passed per unit, unit cell area per unit time is given by

$$J' = \frac{J}{L_{p-p}} = \frac{u}{L_{p-p}^2} \quad (4.2.7)$$

In the specific unit cell shown in Fig 4.2 and Fig 4.3, the angle between the 1<sup>st</sup> particle and the i-th particle is given by

$$\beta_i = \tan^{-1} \left( \frac{x}{L_{p-p}/2} \right) \quad (4.2.8)$$

Where x is called the separating distance, shown in Fig 4.3.  $\beta_i$  is called trailing angle, meaning that only one trench is formed during this  $\beta_i$  angle rotation. Time required for this angle rotation is simply  $\Delta t = \beta_i / \omega$ , where  $\omega$  is the rotational speed of the wafer. Thus the number of particles passing unit cell during time  $\Delta t$  is given by

$$N_\beta = \left( \frac{u}{L_{p-p}} \right) * \Delta t = \left( \frac{u}{L_{p-p}} \right) * \left( \frac{\beta_i}{\omega} \right) \quad (4.2.9)$$

$N_\beta$  can be called inactive number of particles of each train, and  $(N_\beta + 1) * L_{p-p}$  is the length of each inactive train segment. Thus the number of train segments per unit time is given by

$$N_e = \frac{J}{N_\beta + 1} \cong \frac{J}{N_\beta} = \frac{\frac{u}{L_{p-p}}}{\frac{u * \beta}{L_{p-p} * \omega}} = \frac{\omega}{\beta_i} \quad (4.2.10)$$

$N_e$  is essentially the trenches left per unit time. The approximation in Eq (4.2.10) is valid for

$N_\beta \gg 1$ . Then we can write the number of train segments per revolution

$$N_{rev} = N_e * \frac{2\pi}{\omega} = \frac{2\pi}{\beta_t} \quad (4.2.11)$$

In other words,  $N_{rev}$  is the number of trenches left in the unit cell per revolution.

It is assumed that each two trenches in the unit cell will form one and only one intersection, then by simple combination idea, the number of intersections per revolution is given by

$$N_{in-p} = C_{N_{rev}}^2 = \frac{N_{rev}!}{2! * (N_{rev} - 2)!} = \frac{N_{rev} * (N_{rev} - 1)}{2} = \frac{\frac{2\pi}{\beta_t} * \left(\frac{2\pi}{\beta_t} - 1\right)}{2} \quad (4.2.12)$$

Since the above discussion is within the unit cell. Thus, normalized by the area of unit cell area, the number of intersections per revolution per unit area is given by

$$N_{in} = \frac{N_{in-p}}{L_{p-p}^2} = \frac{\frac{\frac{2\pi}{\beta_t} * \left(\frac{2\pi}{\beta_t} - 1\right)}{2}}{\frac{\pi d^2}{6\alpha}} = \frac{\frac{2\pi}{\beta_t} * \left(\frac{2\pi}{\beta_t} - 1\right) * 6\alpha}{2 * \pi d^2} \quad (4.2.13)$$

### 4.2.3 Typical concentration definition

The weight concentration  $\alpha_m$  of slurry is defined as  $W_a / W_{slurry}$ .

If we consider volume  $A_w d$ , which is a mono-layer of particles, then

$$\begin{aligned} A_w d &= Vol_a + Vol_{slurry} = \frac{W_a}{\rho_a} + \frac{W_{slurry}}{\rho_{slurry}} = \frac{W_a}{\rho_a} \left(1 + \frac{\rho_a}{\alpha_m \rho_{slurry}}\right) = Vol_a \left(1 + \frac{\rho_a}{\alpha_m \rho_{slurry}}\right) \\ &= N * \frac{\pi}{6} d^3 \left(1 + \frac{\rho_a}{\alpha_m \rho_{slurry}}\right) \approx N * \frac{\pi}{6} d^3 \frac{\rho_a}{\alpha_m \rho_{slurry}} \end{aligned} \quad (4.2.14)$$

and N is the total number of particles in this volume (or taken as the particles under the wafer). The number of particles per unit area is given by

$$\frac{N}{A_w} = \frac{d}{\frac{\pi}{6} d^3 (1 + \frac{\rho_a}{\alpha_m \rho_{slurry}})} \approx \frac{1}{\frac{\pi}{6} d^2 \frac{\rho_a}{\alpha_m \rho_{slurry}}} . \quad (4.2.15)$$

The number of particles per unit volume is given by

$$\frac{N}{Vol} = \frac{1}{\frac{\pi}{6} d^3 (1 + \frac{\rho_a}{\alpha_m \rho_{slurry}})} \approx \frac{1}{\frac{\pi}{6} d^3 \frac{\rho_a}{\alpha_m \rho_{slurry}}} . \quad (4.2.16)$$

If volume concentration is considered, and it is usually defined as  $\alpha_v = \frac{Vol_a}{Vol_{slurry}}$ .

Then for volume  $A_w d$ ,

$$\begin{aligned} A_w d &= Vol_a + Vol_{slurry} = Vol_a (1 + \frac{1}{\alpha_v}) \\ &= N * \frac{\pi}{6} d^3 (1 + \frac{1}{\alpha_v}) \approx N * \frac{\pi}{6} d^3 \frac{1}{\alpha_v} \end{aligned} \quad (4.2.17)$$

So the number of particles per unit area is given by

$$\frac{N}{A_w} = \frac{d}{\frac{\pi}{6} d^3 (1 + \frac{1}{\alpha_v})} \approx \frac{1}{\frac{\pi}{6} d^2 \frac{1}{\alpha_v}} . \quad (4.2.18)$$

The number of particles per unit volume is given by

$$\frac{N}{Vol} = \frac{1}{\frac{\pi}{6} d^3 (1 + \frac{1}{\alpha_v})} \approx \frac{1}{\frac{\pi}{6} d^3 \frac{1}{\alpha_v}} . \quad (4.2.19)$$

By comparing Eq (4.2.15) to Eq. (4.2.18), the weight concentration can be expressed as volume concentration as  $\alpha_m = \frac{\rho_a}{\rho_l} \alpha_v$ . In real manufacturing process, The number of

abrasive particles per unit volume G is given by

$$\begin{aligned}
 G &= \frac{\frac{W_a}{\rho_a Vol_a}}{Vol_{slurry} + Vol_{water}} = \frac{\frac{W_a}{\rho_a Vol_a}}{Vol_{slurry} + Vol_{water}} * \frac{Vol_{slurry} \rho_{slurry}}{W_{slurry}} \\
 &= \frac{\rho_{slurry}}{\rho_a Vol_a} * \frac{Vol_{slurry}}{Vol_{slurry} + Vol_{water}} * \frac{W_a}{W_{slurry}} = \frac{\rho_{slurry}}{\rho_a \left( \frac{\pi}{6} d^3 \right)} \alpha_s \alpha_m
 \end{aligned} \tag{4.2.20}$$

$\alpha_s$  is the dilution ratio, defined as the ratio of  $Vol_{slurry}$  to the sum of  $Vol_{slurry}$  and  $Vol_{water}$ .

If no water is added, the Eq (4.2.20) is same with Eq (4.2.16) or Eq (4.2.19).

### 4.3 The average local pressure applied on the solid-solid contact region

If an ideal flat and smooth pad surface is assumed, the real applied pressure could be assumed to be equal to the pressure applied on the pad regions containing the active particles.

But this is not the real situation. An industry pad (IC1000) topography structure is shown in Fig 4.4.

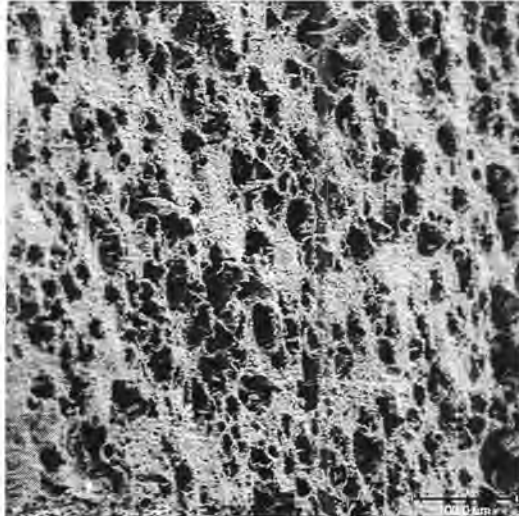


Figure 4.4 SEM image of an IC 1000 pad. The pad surface is tilted 60° to show the relative surface topography.

Based on the recent research Bastawros (2002), it has a cellular structure with inter connected pores. The average pore diameter is about  $d_p = 50\mu m$ , and the pad surface density is about 35%. The pad surface roughness is evaluated by a surface profilometer. A long wavelength is observed with length scale about 15 to 20 times the pore diameter, with amplitude about 0.1 to 0.2 times the pore diameter. It is worth noting that with this long wavelength, there is still a short wavelength that is in the scale of 2 to 4 times the pore diameter. So the applied pressure is support by the high region of the pad. Since the abrasive particles diameter is around 100 nm ranges, only those particles residing in the high regions of the pad is active in cutting the wafer surface material. So the applied pressure is not equal to the pressure applied on the region containing the active particles. A relationship between them should be developed.

#### 4.3.1 Asperity model

A periodic roughness over the pad surface is assumed. The asperity is assumed as a spherical cap with radius R. The contact between the asperity and the wafer surface is taken as Hertz elastic contact problem. The spherical cap is taken as a spherical indenter in this model.

Based on Hertz's elastic contact model for spherical indenter, (as used by Luo and Dornfeld, 2001).

$$a^3 = \frac{3}{4} * \frac{F_{n-in} * R}{E'} \quad (4.3.1)$$

a is the contact radius.

$F_{n-in}$  is the normal force on the indenter,

R is the radius of the asperity that is taken as the radius of indenter.

$$E' = \frac{1}{\frac{1}{E_w} + \frac{1}{E_p}} \text{ is the equivalent elastic modulus.}$$

$E_w$  is the elastic modulus of wafer.

$E_p$  is the elastic modulus of pad.

And number of summits per unit area is given by  $n_{sum}/A_w$ , which is taken as a constant evaluated from experiment.

The force per summit, or the normal force on the indenter is given by

$$F_{n-in} = \frac{P_0 A_w}{n_{sum}} = \frac{P_0}{n_{sum}/A_w} \quad (4.3.2)$$

So the contact radius is given by

$$a = \left( \frac{3}{4} * \frac{P_0 * R}{\frac{n_{sum}}{A_w} E'} \right)^{1/3} \quad (4.3.3)$$

The contact area is given by  $A_{sum} = \pi * a^2 = \pi * \left( \frac{3}{4} * \frac{P_0 * R}{\frac{n_{sum}}{A_w} E'} \right)^{2/3}$ .

The real contact area between wafer and pad is

$$A = A_w * \frac{n_{sum}}{A_w} * A_{sum} = A_w * \frac{n_{sum}}{A_w} * \pi * \left( \frac{3}{4} * \frac{P_0 * R}{\frac{n_{sum}}{A_w} E'} \right)^{2/3} = b A_w = b_1 * \left( \frac{P_0}{E'} \right)^{2/3} A_w \quad (4.3.4)$$

Where  $b_1 = \pi * \left( \frac{3}{4} * \frac{R}{\frac{n_{sum}}{A_w}} \right)^{2/3} * \frac{n_{sum}}{A_w} = const$  is dependent on the pad topography.

The ratio of real contact surface area to the wafer surface area is given by

$$b = b_1 * \left(\frac{P_0}{E'}\right)^{2/3} \quad (4.3.5)$$

If we assume that the force are only transferred by solid-solid contact between wafer and pad.

Based on force equilibrium, the average real local pressure in the asperity is given by

$$P = \frac{P_0 * A_w}{A} = \frac{P_0}{b} = \frac{1}{b_1} (E')^{2/3} * P_0^{1/3} \quad (4.3.6)$$

The assumptions implied in this model is same with Hertz elastic contact model, and also that the pad surface is taken as a periodic spherical shape. It is also assumed that the local pressure is uniform in each asperity. Eq. (4.3.6) is the same as that developed by Luo and Dornfeld (2001).

#### 4.3.2 FEM model

Based on recent research by Bastawros (2002), the relationship between local pressure and the applied pressure is obtained by FEM analysis incorporation nonlinear pad behavior. This may be expressed as,

$$P = \frac{P_0^{1-2n}}{\pi * r_p * \xi_1^2} E_p^{2n} \quad (4.3.7)$$

Where  $\xi_1$  is approximately 0.71 to 1.35, and  $n$  is about 0.3 to 0.37. They are two constants determined from FEM simulation.  $r_p$  is the pad surface density, about 0.35 which is estimated from the SEM image of IC 1000 pad.  $E_p$  is the pad modulus. It is easily seen that the exponent of  $P_0$  in Eq. (4.3.7) is on the order of 0.26 to 0.4, and the Hertz contact model gives the exponent of  $P_0$  for 0.33. So they are comparable to each other.

## 4.4 Normal force per particle

The idea here is that the mean normal force on each particle is simply the mean pressure in the neighboring region of the particles times the non-contact area around each particle for pad-wafer contact mode. For non-contact mode, the mean force on each particle is simply the total force divided by the number of active particles (particles in the real contact area). For contact mode, full contact mode and partial contact model are considered here.

### 4.4.1 Full contact model

If the diameter of the non-contact area is simply assumed as the average particle diameter.

The normal force on each particle is approximately given as

$$F_n = \frac{\pi}{4} P l^2 \quad (4.4.1)$$

Where  $l = d$ , and  $d$  is the average particle diameter of particles. Such conditions exist when the pad is very soft, the particle concentration is low and the pressure is very high.

### 4.4.2 Partial contact model

There is an intermediate state between non-contact model and full contact mode, partial contact mode. And this mode is supposed to be the most usual case during polishing process.

It is characterized by non-contact domain length  $l$ , which is not equal to the particle diameter.

According to FEM results (Bastawros, 2002), the normal force is given by

$$F_n = \frac{\pi}{4} \xi_3 P l^2 \quad (4.4.2)$$

Where  $\xi_3 \approx 1.55$  account for the edge effect.

Non-contact length  $l$  is given by (Bastawros, 2002),

$$l = d * (\xi_2 \xi_1^{2m} \pi^m) r_p^m \left( \frac{E_p}{P_0} \right)^{m(1-2n)} \quad (4.4.3)$$

Where  $\xi_2 \approx 1.1$ ,  $m \approx 0.42$ , is determined by FEM simulation.

#### 4.4.3 Beam model

Based on Fu et al (2001), the pad behaves like a beam. And the particles are assumed uniformly distributed, and the inter-particle length is taken as the beam length. For contact mode, the normal force per particle is given by

$$\begin{aligned} F_n &= \left( \frac{4^5}{3^3} \right)^{1/4} (E_p t_p^3 \frac{d}{2} \left( \frac{A}{N} \right)^2 P^3)^{1/4} \\ &= \text{const1} * d^{5/4} * P^{3/4} \\ &= \text{const2} * \left( \frac{A}{N} \right)^{5/8} * P^{3/4} \end{aligned} \quad (4.4.4)$$

Where  $t_p$  is the pad thickness.

The limitations of this model is that it is not really physically a beam, since the beam length is in the order of sub-micro size, and the beam thickness is in the order of several microns. But the predicted MRR using this model matches very well with some experimental data.

### 4.5 Indentation depth of a single particle

In this step, the penetration depth of a single particle can be derived if the force per particle is given. Actually the indentation depth is a very important parameter in surface polishing process.

#### 4.5.1 Perfect plasticity model (Plastic contact and small indentation):

If the material is taken as perfect plastic material, and there is no friction in the particle-wafer

interface. Referring to Fu et al (2001), the indentation depth is given by

$$h = \frac{F_n}{\pi * \sigma_y * d} \quad (4.5.1)$$

Where  $\sigma_y$  is yield strength of material, h is the indentation depth.

#### 4.5.2 Hardness test model

During the hardness test, one method for measuring the hardness is to measure the contact radius a under certain load. The hardness is defined as

$$H = \frac{F_n}{\pi * a^2} \quad (4.5.2)$$

For small indentation depth, contact radius is given by  $a = \sqrt{d * h}$ .

So hardness can be assumed as  $H = \frac{F_n}{\pi * d * h}$ .

If a sliding indentation condition is considered, only the front area of the indenter is in contact with the specimen, so the contact area is half of the contact area under static condition.

So hardness can be taken as  $H = \frac{2F_n}{\pi * d * h}$ .

And indentation depth is given by

$$h = \frac{2F_n}{\pi * d * H} \quad (4.5.3)$$

For general material (like metal), the relation between hardness and yield strength of the material is given by  $H = 3\sigma_y$ . By comparing Eq (4.5.3) with Eq. (4.5.1), there is no much difference between the above two models. These models are mainly used for some metals

(perfect plasticity could be assumed), and spherical indenter.

#### 4.6 Tangential force acting on the active particles.

The tangential force is generated during the horizontal motion of the particles. It can be used to determine the characteristic length during the intersection of two scratches by using force equilibrium or work balance.

##### 4.6.1 Model based on orthogonal cutting

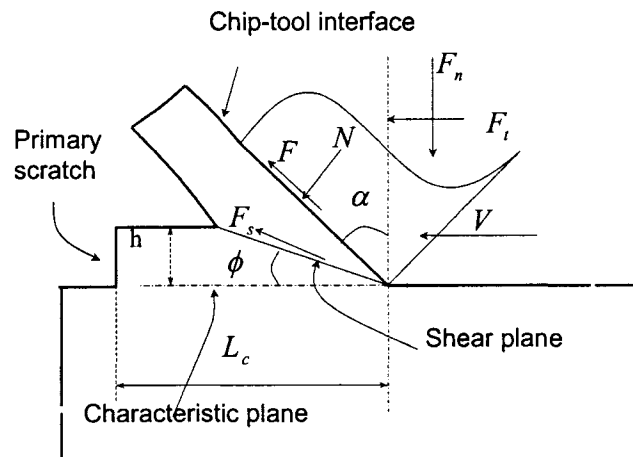


Figure 4.5 Orthogonal cutting process shows that two mechanism of ploughing and shearing.

The intent of this work is to eventually develop a model for MRR prediction in a nano-scale polishing or CMP process. In a typical polishing process, the down pressure is known. Utilizing the approach of Fu et al (2001), Luo and Dornfeld (2001) or Bastawros et al (2002), and determining the contact regime (no contact, partial contact or full contact between pad and wafer), the normal force  $F_n$  per abrasive particle may be determined. In our

current experimentation, the indenter represents a single abrasive particle, and the normal force  $F_n$  on it will be known from process conditions. Knowing  $F_n$ ,  $F_t$  can be estimated using orthogonal metal cutting theory (e.g. Shaw 1984).

Referring to Fig 5, we may write

$$F_s = F_t \cos \phi - F_n \sin \phi \quad (4.6.1)$$

When  $F_s$  is the shear force on the shear plane and  $\phi$  is the shear angle. Assuming a perfectly plastic material, we may estimate  $F_s$  to be

$$F_s = \tau_{flow} * A_s = \tau_{flow} * \frac{wh}{\sin \phi} \quad (4.6.2)$$

When  $\tau_{flow}$  is the shear flow strength of the material,  $w$  is the width of cut and  $h$  is the depth of cut, and  $A_s$  is the area of the shear plane. Then  $F_t$  may be expressed as

$$F_t = \frac{\tau_{flow} * \frac{wh}{\sin \phi} + F_n * \sin \phi}{\cos \phi} \quad (4.6.3)$$

and an iterative method may be used to determine the tangential force.

Iteration steps:

1. Use experimentally determined  $F_n$ . Alternatively,  $F_n$  may also be estimated as normal force per particle from the prescribed down pressure in a polishing process.
2. Assume a shear angle value, (usually within  $10^\circ$  to  $25^\circ$ ).
3. Find  $F_t$  value based on eqn. (4).
4. Find the  $F_t/F_n$  ratio.
5. Find the friction angle on the chip-tool plane as,

$$\beta = \tan^{-1} \left( \frac{\frac{F_t}{F_n} \tan \alpha + 1}{\frac{F_t}{F_n} - \tan \alpha} \right), \text{ where } \alpha \text{ is the rake angle.}$$

6. Obtain shear angle  $\phi$  based on the principle of minimum energy,

$$\phi = \left( \frac{\pi}{4} + \frac{\alpha}{2} \right) - \frac{\beta}{2} \quad (4.6.4)$$

and check for convergence of shear angle  $\phi$ .

The  $F_t$  value when convergence of  $\phi$  is obtained is the desired estimate of the tangential force during the scratching process when the indenter of the tool is far away from the edge of the primary scratch. This  $F_t$  value represents the maximum  $F_t$  that can be supported by a perfectly plastic material before the material will fail at the shear plane.

Table 5 Comparison for different assumptions

| Assumed $\tau_{flow}$ (MPa)         | $w$   | Converged $\phi$ (deg) | $\beta$ (deg) | $F_t$ (estimate) (N) |
|-------------------------------------|-------|------------------------|---------------|----------------------|
| $\tau_y = \frac{70}{\sqrt{3}}$      | $2h$  | 3.9                    | 37.2          | 0.342                |
| $\tau_{ult} = \frac{220}{\sqrt{3}}$ | $2h$  | 6.9                    | 31.3          | 0.61                 |
| $\tau_y = \frac{70}{\sqrt{3}}$      | $10h$ | 8.6                    | 27.8          | 0.772                |
| $\tau_{ult} = \frac{220}{\sqrt{3}}$ | $10h$ | 14.6                   | 15.7          | 1.401                |

Experimental values:  $h = 12 \mu m$ ,  $\alpha = -45^\circ$ ,  $F_n = 2.5 N$ ,  $F_t = 1.2 N$ .

As an intermediate check, we compared the experimental  $F_t$  value to the estimate of  $F_t$ .

Table 5 shows the comparison for different assumptions.  $\tau_{flow}$  can be assumed to be either the initial shear yield strength or the shear ultimate strength of copper. To be consistent with plane strain assumption in orthogonal metal cutting theory,  $w$  should be large compared to  $h$ . However, in the experiment, it is a conical indenter with an included angle of  $90^\circ$ . So  $w$  may be estimated as  $w = 2h \tan(\alpha)$  or  $w = 2h$  for this indenter. Accordingly, we tried  $w = 2h$  and  $w = 10h$ . Since, the estimated  $F_t$  comes closest to experimental value for

$\tau_{flow} = \tau_{ult} = \frac{220}{\sqrt{3}} MPa$  and  $w = 10h$ , these estimates are adopted for later calculation.

#### 4.6.2 Experimental model

Based on the cross-scratch experiment, the ratio of tangential force to normal force can be taken as a constant for each scratch.

So tangential force is given by

$$F_t = \mu' F_n \quad (4.6.5)$$

$\mu'$  is a constant (in the range of 0.2 to 0.4 for sliding indentation in pure copper) determined from the experiment. The good aspect of this model is simple and practical, but the experimental work has to be done for each specific material under certain conditions.

### 4.7 Characteristic length during the intersections at right angle

#### 4.7.1 A simple mechanistic model

Referring to Fig 4.5, we propose a very simple shear failure mechanism, where shear failure occurs along a horizontal plane extending from the indenter to the edge of the primary scratch before shear localization can take place according to traditional metal cutting theory.

Then

$$F_t = \tau_{flow} * w * L_c \quad (4.7.1)$$

Assuming  $\tau_{flow} = \frac{220}{\sqrt{3}}$  and  $w=10h$  for  $h = 12\mu m$ , we get  $L_c = 7.6h$  for  $F_t = 1.4N$ .

The simple shear failure criterion used in the analytical model predicts  $L_c$  to be around  $7.6h$  for the experimental conditions on copper, which is of the same order, but still significantly higher than the experimental value. There may be several reasons for this discrepancy:

1. Only the shear failure along the bottom plane is considered in the analytical model. For the conical indenter in the experiment, the surface of shear failure may be inclined and different.
2. The assumption  $w = 10h$  to represent plane strain is approximate.
3. The material may be strain hardening due to the deformation induced by the scratching process, while only a perfect plasticity assumption is used in the present analytical model. Utilization of strain gradient plasticity may also be appropriate for the small depth of cut used in the experiment.
4. For the conical indenter with included angle  $90^\circ$  and  $5\mu m$  nose radius, oblique cutting theory may be more appropriate at  $1 - 30\mu m$  depth of cut.

Work is currently in progress to develop a MRR prediction model for the CMP process based on the concept of material detachment due to scratch intersection.

#### 4.7.2 FEM result.

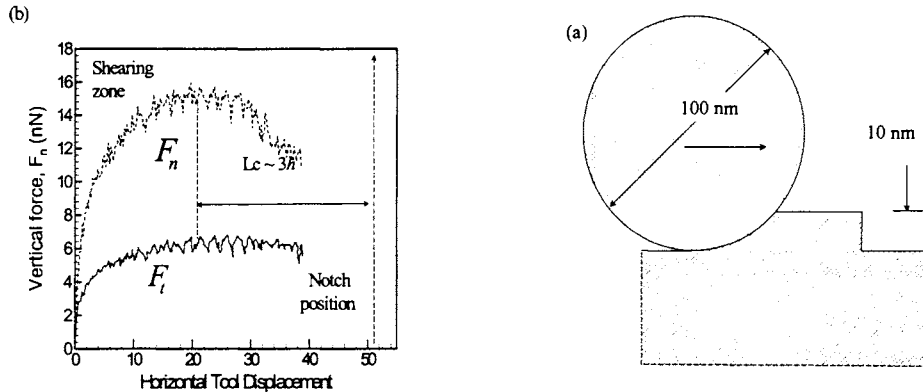


Figure 4.6 (a) FEM abrasive particle-surface interaction model. (b) Normal and tangential reaction forces on the abrasive particles.

The intersecting scratch concept for the material detachment mechanism is examined by finite element simulation using ABAQUS/Explicit package. The implemented 2-D plane strain model is shown in Fig. 6(a), where a recess in the surface is made ahead of the abrasive particle and equal to the initial depth of cut to simulate the intersection with the primary scratch. The abrasive particle is assumed rigid while the ploughed surface has material parameters consistent to those for copper ( $E=109.2\text{GPa}$ ,  $\sigma_y=69\text{MPa}$ ,  $\sigma_{ult}=258.2\text{MPa}$ ). An isotropic elastic strain hardening material model is used with hardening exponent  $n=0.2$ . No friction is considered between the particle and substrate. The simulation proceeded by translating the particle horizontally at a constant speed of  $0.1\text{ m/s}$ . Typical reaction forces on the abrasive particles are shown on Fig. 6(b) against the sliding distance for a depth of cut of  $10\text{nm}$ . Away from the surface recess, the ratio of  $F_t/F_n$  is approximately  $0.37$ . The normal reaction  $F_n$  starts to drop at a distance of approximately  $3$  times  $h$ , however, the decay of  $F_t$

was not substantial. Utilization of cohesive elements with traction separation law should provide better clarification for the tangential force decay. The simulation consistently showed the length of the shearing zone  $L_c$  to be between  $3h$  and  $4h$ .

## 4.8 Volume per intersection

Using Eq. (4.7.7), the volume per intersection is given by

$$V_{in} = L_c * A_c = L_c * \frac{2}{3} * 2\sqrt{dh} * h = \frac{4C}{3} * d^{0.5} * h^{2.5} \quad (4.8.1)$$

In the above equation, it is assumed that the indentation depth is small compared with the spherical particle diameter, and then use parabolic approximation to calculate the cross-section area.

The early MRR model assumes that all the material in the trench is removed. The volume is taken as the product of the cross-section area of the scratch with the velocity of the particle, which is quite different with this model.

## 4.9 MRR model

The existing model is described in section 4.9.1, and our new intersection model is elaborated in section 4.9.2.

### 4.9.1 Existing MRR model

The material removal rate is usually defined as

$$MRR = \frac{dH}{dt} = \frac{N * A_c * u}{A_w} \quad (4.9.1)$$

Where  $A_c$  is the cross-section area of the groove made by a single abrasive,  $u$  is the linear

velocity of the particle, and N is taken as the active particle numbers here.

#### 4.9.2 Present Intersection model

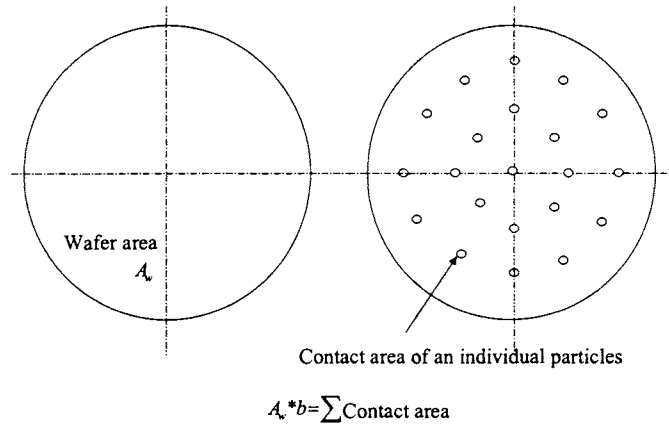


Figure 4.7 A schematic of wafer pad contact area.

Based on our cross-scratch experiment, it is more reasonable to apply our new observed material removal mechanism to the MRR model. And the MRR should be corrected as

$$MRR = \frac{dH}{dt} = \frac{(N_{in} * \omega * (A_w * b)) * V_{in}}{A_w} = (N_{in} * \omega * b) * V_{in} \quad (4.9.2)$$

Where  $N_{in}$  is the number of intersections per revolution per unit area,  $V_{in}$  is the volume for each intersection,  $\omega$  is the revolution per unit time,  $b$  is the ratio of real contact area to wafer area.  $N_{in} * \omega * (A_w * b)$  is simply the number of intersections per unit time in the real contact area between wafer and pad. The schematic of contact area is shown in Fig 4.7.

By combining Eq. (4.8.1) with Eq. (4.5.1), volume per intersection is given by

$$V_{in} = l_c * A_c = l_c * \frac{2}{3} * 2\sqrt{dh} * h = \frac{4C}{3} * d^{0.5} * \left( \frac{F_n}{\pi\sigma_y d} \right)^{2.5} = \frac{4C}{3\pi^{2.5}} * \frac{1}{d^2} * \left( \frac{F_n}{\sigma_y} \right)^{2.5} \quad (4.9.3)$$

By applying Eq. (4.3.7), (4.4.2) and (4.4.3), we have

$$\begin{aligned} F_n &= \frac{\pi}{4} \xi_3 \frac{P_0^{1-2n}}{\pi * r_p * \xi_1^2} E_p^{2n} \left( \left( \xi_2 \xi_1^{2m} \pi \right) r_p^m \left( \frac{E_p}{P_0} \right)^{m(1-2n)} \right)^2 \\ &= \frac{\pi^{2m} \xi_2^2 \xi_3}{4 \xi_1^2} * \frac{d^2 E_p^{2(n-2nm+m)} P_0^{1-2(n-2nm+m)}}{r_p^{1-2m}} \end{aligned} \quad (4.9.4)$$

It can be rewritten as  $F_n = 2d^2 E_p^{0.9376} P_0^{0.0624}$  by applying those parameters determined from FEM simulation (See section 4.3.2 and section 4.4.2).

So the volume per intersection can be simplified as

$$V_{in} = 1.8d^3 E_p^{2.344} P_0^{0.156} * \left( \frac{1}{\sigma_y} \right)^{2.5} \quad (4.9.5)$$

The real contact area ratio  $b$  is given by (refer to Eq. (4.3.7))

$$b = \frac{P_0}{P} = \frac{P_0}{\frac{P_0^{1-2n}}{\pi * r_p * \xi_1^2} E_p^{2n}} \cong 0.6 \left( \frac{P_0}{E_p} \right)^{0.74} \quad (4.9.6)$$

The number of intersections per revolution per unit area is given by Eq. (4.2.13).

So The MRR is given by

$$\begin{aligned} MRR &= N_{in} * \omega * b * V_{in} \\ &= \frac{2\pi * \left( \frac{2\pi}{\beta_i} - 1 \right) * 6\alpha}{2 * \pi d^2} * 1.8d^3 E_p^{2.344} P_0^{0.156} * \left( \frac{1}{\sigma_y} \right)^{2.5} * 0.6 \left( \frac{P_0}{E_p} \right)^{0.74} * \omega \\ &= \frac{2\pi}{\beta_i} * \left( \frac{2\pi}{\beta_i} - 1 \right) * \alpha * d * \left( \frac{1}{\sigma_y} \right)^{2.5} * E_p^{1.6} P_0^{0.9} * \omega \end{aligned} \quad (4.9.7)$$

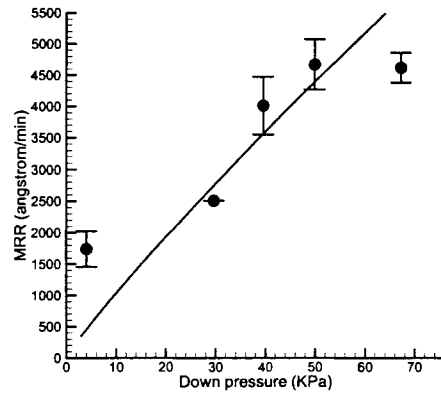


Figure 4.8 Comparison between model predictions and the copper CMP data with pressure.

By applying the experimental data for the parameters of the above equation, the predicted amplitude of MRR becomes comparable to those measured in experiments. The comparisons with pressure and velocity are shown in Fig 4.6 and Fig 4.7 respectively. The solid line is the model prediction, and the symbols with error bar are experimental data (Luo et al, 1998).

The applied parameters from experimental data for copper film are elaborated below. Rotation speed is  $\omega = 35 \text{ rev/min}$  (relative to 16.8m/min) for Fig 4.6, down pressure is  $P_0 = 30 \text{ KPa}$  for Fig 4.9, volume concentration is  $\alpha = 0.0125$  (relative to weight concentration  $\alpha_m = 0.05$ ), the diameter of  $\alpha$ -alumina particles 100nm. And for pure copper, yield strength is  $\sigma_y = 70 \text{ MPa}$  (no softening is considered), the pad modulus is taken as  $E_p = 180 \text{ MPa}$  based on Bastawros (2002). The trailing angle is taken as approximately in the range of  $9^\circ$  to  $10^\circ$ , and the predicted material removal rate is approximately same as experiment data (Luo et al, 1998).

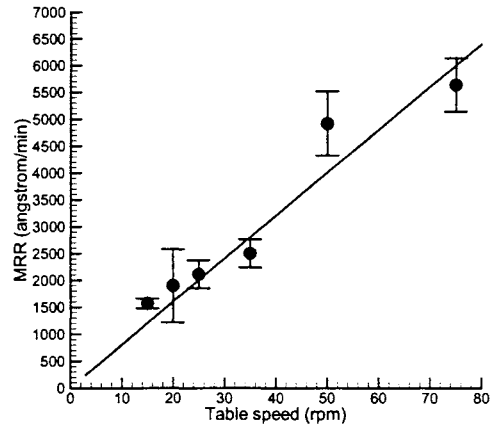


Figure 4.9 Comparison between model predictions and the copper CMP data with velocity.

If the trailing angle is taken as  $6^\circ$ , which is estimated by assuming that the separating distance is same with the trench width, then the ratio of model prediction of MRR to the experimental MRR data for copper is about 3 times. If the trailing angle is taken as  $30^\circ$ , then the ratio of model prediction of MRR to the experimental MRR data for copper is about 1/6. So the predicted MRR of this physical model is comparable to real experimental data, and also the trends with pressure and velocity are similar to Preston's equation. The other parameters in Eq. (4.9.7) can be taken as the Preston's coefficients.

## Chapter 5 Conclusion and Future Work

### 5.1 Conclusion

The surface material detachment of pure copper surface is studied experimentally by a micro-scale scratch experiment. The observed deformation pattern through SEM image and the trends of measured force profile reveal that the material is primarily ploughed along a single scratch, and there is no net surface material detached. It is also observed that the deformation mechanism of pure copper under sliding indentation changes from steady ploughing mode to shearing mode close to the intersection of two scratches, and a segment of material is sheared off. The characteristic length of this segment is found to be of the order of the indentation depth based on the experimental observation. To understand the mechanical base for this characteristic length, a simple energy comparison between shearing and ploughing is performed. It is found that the theoretical model prediction for this characteristic length is comparable to the experimental result. So the proposed mechanism for surface material detachments under microns or sub-microns indentation depth for ductile metals is justified.

The framework involved in the MRR model development during CMP process is proposed. The different physical based model for each step in the framework is discussed. A mechanism-based MRR model is developed based on this surface detachment idea. The Bastawros et al (2002) FEM simulation results for the load magnitude due to pad surface asperities have been integrated into this new model. It is found that the predicted magnitude of MRR is comparable to the experimental data for copper by Luo et al (1998). The trends of

MRR with pressure, velocity, and particle concentration match very well with experimental data.

## 5.2 Future Work

The current work is focusing on the material removal mechanism under abrasive particle abrasion in micro-range, and then applying the gained insights to a mechanism-based MRR model.

The first step of future work is extending the cross-scratch experiment to nano-range. Since the indentation depth of abrasive particles is estimated to be in the range of a few nanometers during CMP process, the investigation of the material removal mechanism in nano-range will give more plausible explanation by experimental method. The relation between indentation depth and normal force, and the ratio of tangential force to normal force will be got in nano-range through single indent and single scratch experiment.

The second step of future work will consider the chemical effect during the CMP process. Since the early work always deal with the mechanical and chemical effects separately, the interactive effects by them have not been studied. So what's the material removal mechanism under both the mechanical and chemical effects will be a major work of next step. The specific study will also focus on the material for the connector of multilevel layers, like pure copper.

The third step of future work will consider the patterned wafer, not only the blank wafer. From the industry view, all the wafers are patterned. And the patterns can be characterized as different line-width. So the wafer surface needed to be planarized will have a step height (involving high feature and low feature polishing). The different material removal

mechanism and MRR model should be developed under such features.

Although the study is limited to pure copper, it should be extended to different materials, such as metals (like aluminum, tungsten), and semiconductor (like silicon oxide).

The gained insights in material removal mechanism and the MRR model built for CMP process should be integrated into some kinds of software. The software can be used to predict the MRR under different conditions, including complex surface topography, different operational parameters (like particle size and shape, particle concentration, down pressure and rotational speed), different slurries and so on.

## References

1. Bastawros, A-F, Chandra, A., Guo, Y., Yan, B., 2002, Pad Effects on Material Removal Rate in Chemical Mechanical Planarization, (Submitted).
2. Brown, N.J., 1987, Some Speculations on the Mechanisms of Abrasive Grinding and Polishing, *Precision Engineering*, Vol. 9, No. 3, pp. 129-138.
3. Brown, N.J., Baker, P.C. and Maney, R. T., 1981, Optical polishing of metals, *Proc. of SPIE*, Vol. 306, pp. 42-57.
4. Bulsara, V.H., Ahn, Y., Chandrasekar, S. and Farris, T.N., 1997, Mechanics of Polishing, *Manufacturing Science and technology*, ASME, Vol. 1, pp. 225-233.
5. Che, W., Guo, Y., Bastawros, A.Chandra, A., 2002, Mechanistic Understanding of Material Detachment During CMP Process, (Submitted).
6. Fu, G., Chandra, A., Guha, S. and Subhash, G., 2001, A plasticity based model of material removal in chemical mechanical Polishing (CMP), *IEEE Trans. Semiconductor. MFG.*, Vol. 14, no. 4, pp. 406-417.
7. Gahlin, R., Axen, A. and Jacobson, S., 1998, The influence of tip shape in abrasion studied by controlled multiasperity surfaces, *Wear*, Vol. 223, pp. 150-156.
8. Kalpakjian, S. and Schmid, S., 2001, *Manufacturing Engineering and Technology*, Prentice-Hall, UK, 4<sup>th</sup> Ed..
9. Luo, J. and Dronfeld, D.A., 2001, Material removal mechanism in chemical mechanical polishing: theory and modeling, *IEEE Trans. Semiconductor. MFG.*, Vol. 14, no. 2, pp. 112-133
10. Luo, Q., Ramaranjan, JS. And Babu, S., 1998, Modification of the Preston equation

- for the chemical-mechanical polishing of copper, *Thin Solid Films*, Vol. 335, pp.160-167.
11. Hill, R., 1983, *The Mathematical Theory of Plasticity*, Oxford University Press.
  12. Hokkirigawa, K. and Kato, K., 1988, Experimental and theoretical investigation of ploughing, cutting and wedge formation during abrasive wear, *Tribology International*, Vol. 21, pp. 151-157.
  13. Ouma, D.O., 1998, Modeling of chemical mechanical polishing for dielectric planarization, Massachusetts Institute of Technology, Dept. Electrical Engineering and Computer Science, Ph.D. Thesis.
  14. Preston, F.W., 1927, The theory and design of plate glass polishing machine, *J. Soc. Glass Tech.*, Vol. 11, no. 44, pp. 214-256.
  15. Shi, E.G., Zhao, B., 1998, Modeling of chemical-mechanical polishing with soft pads, *Appl. Phys. A* 67, pp. 249-252.
  16. Tomozawa, M., 1997, Oxide CMP mechanisms, *Solid State Tech.*, Vol. 40, No. 7, pp 169-175.
  17. Tseng, W.T. and Wang, Y.L., 1997, Re-examination of Pressure and Speed Dependences of Removal Rate During Chemical-Mechanical Polishing processes, *J. Electrochem. Soc.*, Vol. 144, no 2, pp. L15-L17.
  18. Zhao, X. and Bhushan, B., 1998, Material removal mechanisms of single crystal silicon on nanoscale and ultra-low loads, *Wear*, Vol. 223, pp. 66-78.
  19. Zhao, B., and Shi, F. G., 2000, Chemical mechanical polishing in IC processes: new fundamental insights, *Int. J. CMP*, Vol. 1, no. 1, pp. 13-25.
  20. Ye, Y., Biswas, R., Morris, J., Bastawros, A-F, Chandra, A., 2001, Molecular

dynamics simulation of deformation and thermal fields in nano-scratching of copper,

J. Nano Technology, (Submitted).

## Acknowledgement

I will keep the diploma but many share the credit for this work.

First I would like to thank my major professors Abhijit Chandra and Ashraf Bastawros, who have always given me all the support and affirmation of confidence that a graduate student could ask for. I really appreciate their patience and instructions over the past two years. From them I learned the basics of graduate research and how to probe things deeply. And they are always a constant source of inspiration and wisdom.

Here at Iowa State University, I'd like to thank Professor Palaniappa A. Molian for being my thesis reader. I am also thankful for his permission for me to audit his undergraduate lecture, which increases my understanding of basic ideas in manufacturing.

I must thank Dr. Guo and Dr. Fu in our group, who have been giving me support and encouragement. I also must thank my wife who gives me help every day and helps me to release "the stress" which would have otherwise left me frustrated.

For their support and sacrifice, I dedicate this work to them.

This research is supported by Carver Foundation and the Institute for Physical Research and Technology at Iowa State University, Iowa, and by US-NSF grant No. (DMI-0084736).